

Light Water Reactor Sustainability Program

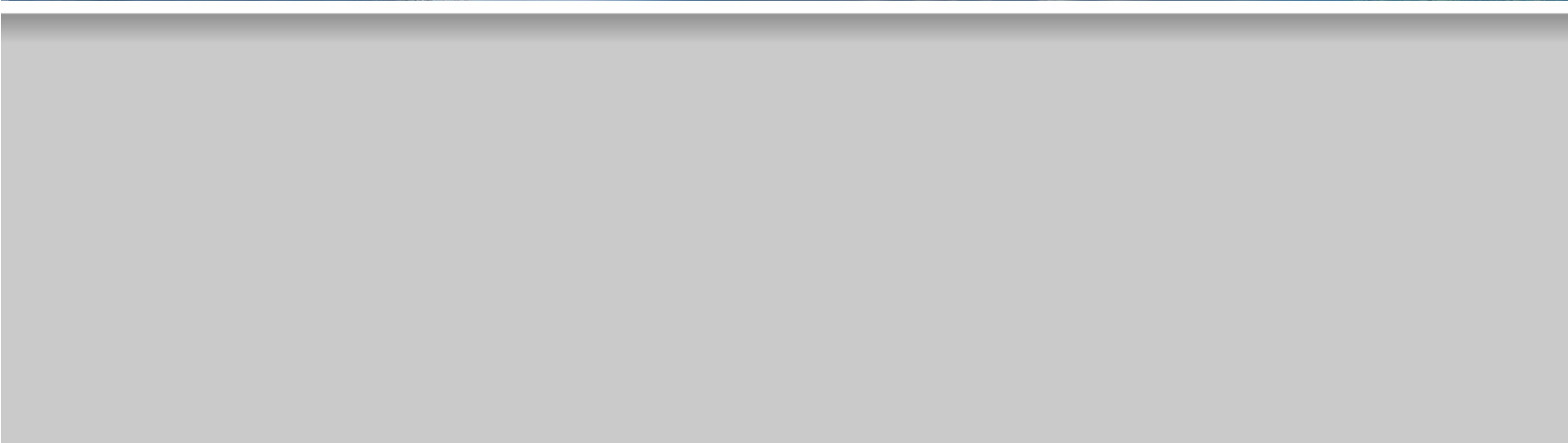
Identification of Mechanisms to Study Alkali-Silica Reaction Effects on Stress-Confined Concrete Nuclear Thick Structures:
Interpretation of the Complete Monitoring Data and Nondestructive Evaluation of the Alkali-Silica Reaction Test Assembly



August 2018

U.S. Department of Energy

Office of Nuclear Energy



DISCLAIMER

This information was prepared as an account of work sponsored by an agency of the U.S. Government. Neither the U.S. Government nor any agency thereof, nor any of their employees, makes any warranty, expressed or implied, or assumes any legal liability or responsibility for the accuracy, completeness, or usefulness, of any information, apparatus, product, or process disclosed, or represents that its use would not infringe privately owned rights. References herein to any specific commercial product, process, or service by trade name, trade mark, manufacturer, or otherwise, does not necessarily constitute or imply its endorsement, recommendation, or favoring by the U.S. Government or any agency thereof. The views and opinions of authors expressed herein do not necessarily state or reflect those of the U.S. Government or any agency thereof.

**Identification of Mechanisms to Study Alkali-Silica Reaction Effects on Stress-
Confined Concrete Nuclear Thick Structures: Interpretation of the Complete
Monitoring Data and Nondestructive Evaluation of the Alkali-Silica Reaction Test
Assembly**

**Nolan Hayes,
Sihem Le Pape,
Z. John Ma
and
Yann Le Pape**

August 2018

M3LW-18OR0403064

**Prepared for the
U.S. Department of Energy
Office of Nuclear Energy**

EXECUTIVE SUMMARY

Context: The Alkali-Silica Reaction (ASR) was discovered by Stanton of the California Division of Highways in 1940. Since then, it has been recognized as a major degradation mechanism for concrete dams. The internal swelling mechanism causes pattern cracking and loss of mechanical properties. There are no known economically viable solutions to prevent the reaction once started. The efficiency of the mitigation strategies for ASR subjected structures is limited. Disclosures of ASR in nuclear generating stations have been made public in Japan and Canada at Gentilly 2 NPP. More recently, in the United States for which the U.S. Nuclear Regulatory Commission issued Information Notice (IN) 2011-20, 'Concrete Degradation by Alkali Silica Reaction,' on November 18, 2011, to provide the industry with information related to the ASR identified at Seabrook. Considering that US commercial reactors in operation are entering the age where ASR degradation can be visually detected and that numerous nonnuclear infrastructures (transportation, energy production) have already experienced ASR in a large majority of States, the susceptibility and significance of ASR for nuclear concrete structures must be addressed in the perspective of license renewal and long-term operation beyond 60 years.

Objectives: Because of exposure, dimension and reinforcement ratio differences, the evaluation of the structural significance of ASR on affected concrete in nuclear power plants cannot be directly transposed from the transportation infrastructures or concrete dams though the methodological pathways are similar to a large extent. The absence of shear reinforcement (i.e. in the thickness) is common resulting in an absence of confinement that favors the out-of-plane ASR expansion. The shear bearing capacity of such concrete structures relies primarily on plain concrete in the bulk. **The residual shear capacity of ASR-affected structures like the biological shield building, the containment building and the fuel handling building will depend on two competing mechanisms: (i) the extent and orientation of the ASR-induced micro-cracking favoring the propagation of a shear fracture and (ii) the relative in-plane confinement-induced compression in the direction of the reinforcement potentially limiting the propagation of the fracture.**

Additionally, effective aging management programs of ASR-affected structure require supplemental monitoring beyond simple visual observation. The practical implementation, the reliability and effectiveness, i.e., significance to capture the ASR-induced damage, of different sensing systems need to be evaluated.

Research Activities: To address these questions, the LWRS Program has developed in partnership with the University of Tennessee, a large-scale testing program on ASR-affected reinforced concrete structural elements representative of structural members found in nuclear power plants. Three concrete specimens were cast and placed within a controlled environmental chamber. The concrete used for these specimens was designed to experience large ASR expansion ($> 0.15\%$) within one year. Each of the three specimens is heavily instrumented with multiple types of sensors measuring deformation, strain, temperature and internal pressure. These specimens are being subjected to ASR for a period of a minimum of two years. After the period of allowed reaction, the specimens will be mechanically tested to observe the effects of

ASR on their shear capacity.

During the monitoring phase, chronic nondestructive evaluation was performed by several partner universities.

Results: This report documents the data and results obtained after one-year of monitoring using multiple types of sensors, visual inspection and passive and active acoustic-wave-propagation-based nondestructive techniques. The main results of this research are:

1. Very good correlation between the fiber-optics-based ~1.0-1.5m long-gauge deformation sensors and embedded strain gauge transducers is observed providing high confidence in the obtained data. Moreover, the high survival rate of the hundreds of the surface and embedded sensors despite the severe operating environment (room temperature 38°C, relative humidity >90%, high alkali content) shows that with proper implementation, such monitoring system can successfully be used in the field.
2. The development of visible ASR-induced cracking appears first and continues developing on the unreinforced lateral sides of the reactive unconfined specimens, in the form of cracks mostly oriented parallel to the reinforced direction. The top and bottom surfaces, of the specimens i.e., covering the reinforcement, show almost no cracking. This observation is critical for in-field assessment where only the face covering the reinforcement is visually accessible. **The absence of visible ASR-induced surface cracking does not imply the absence of ASR-induced deformation and damage in the inaccessible structural concrete.** Because the vast majority of cracks form within the through-thickness plane of the wall, it may be unreliable to depend on the inspection of the visible surfaces of nuclear power plant concrete structures for the early detection of alkali-silica reaction.
3. Due to the absence of transverse reinforcement the ASR-induced expansion occurs primarily in the unreinforced direction, i.e., that of the specimen/wall thickness, resulting in highly anisotropic damage. Companion material mechanical testing on confined and unconfined cylinders, i.e., exhibiting anisotropic and isotropic (pattern) cracking respectively, show significant difference in Young modulus and tensile strength, for the same levels of expansion. **Consequently, mechanical testing of in-situ concrete cored specimens, i.e. with the main axis perpendicular to the reinforcement layout, cannot be directly compared to literature data obtained on ‘free-expansion’ tests.**
4. While the presence of reinforcement reduces considerably the ASR-expansion in the direction of the reinforcement and results in augmented expansion in the unconfined direction, the structural boundary conditions, always present in the field, also plays a significant role in the redistribution of the observed expansion: e.g., the confined specimen exhibits about 30% more expansion in the specimen thickness direction than the unconfined specimen. Hence, careful consideration on the effects of the structural boundary conditions must be taken for the interpretation of the significance of structural laboratory test results to actual in-field structures.
5. **Nondestructive evaluation provides (semi-)quantitative estimates of the ASR-induced damage and expansion:**
 - a. Nonlinear ultrasonic (NLU) Rayleigh surface waves - Georgia Institute of Technology - are extremely sensitive to ASR-induced cracking near the surface (penetration depth in about 2-3 inches) and hence, is indicative of ASR formation assuming that a baseline on sound undegraded concrete can be obtained. It must be emphasized that other degradation mechanisms including carbonation may also cause rapid modification of the nonlinearity parameter leading to more complicated interpretation.

- b. The full capabilities of Diffuse ultrasonic waves (DUW) technique - University of Nebraska Lincoln - through the thickness of the mockup could not be assessed extensively due to a late start. However, the relative wave velocities show an interesting linear relation with transient temperature change suggesting that it can potentially be correlated to the ASR-induced mechanical damage (the acoustic velocity and apparent elastic modulus being related).
- c. The Digital image correlation (DIC) - Vanderbilt University - provided the surface strain fields which averaged values appear to overestimate the deformation measured at different locations between the two layers of reinforcement. It is not clear at this point whether this discrepancy is caused by surface effects or data interpretation (DIC software in particular). Further DIC assessment is planned during the specimens destructive testing.
- d. Acoustic emission (AE) - University of South Carolina - monitoring provides a first-order correlation with the average ASR-induced expansion when calculating the cumulated signal strength (CSS).

Perspectives: This project is entering its final stage: The environmental chamber will be removed and the large-scale specimens will be cut to create a series of structural members to be tested destructively.

While several acoustic waves propagation-based nondestructive techniques are readily available, it must be stressed that there is an important gap of knowledge regarding the use of these techniques as assessment tools for ASR-damage in the sense of structural modeling such as developed in GRIZZLY. The concept of ‘damage characterization’ varies from one techniques to the others, and in general, the ‘damage’ parameter output is not directly comparable with the damage in the sense of continuum mechanics. A significant research effort is needed to address this question by studying the propagation of acoustic waves in cracked mediums at the material’ scale.

ACKNOWLEDGEMENTS

Fiber optic sensor installation, setup, data collection and data analysis are being performed cooperatively by Roberto Lenarduzzi, Dianne Bull, and Corey Singleton of Oak Ridge National Laboratory.

Acoustic emission sensor installation, setup, data collection and data analysis are being performed cooperatively by Paul Ziehl, Rafal Anay, and Vafa Soltangharai of the University of South Carolina.

Digital image correlation setup, data collection and data analysis are being performed cooperatively by Sankaran Mahadevan, Garrett Thorne, David Koester, and Kyle Neal of Vanderbilt University.

Nonlinear Rayleigh surface waves method setup, data collection and data analysis are being performed cooperatively by Larry Jacobs, Gun Kim, and Sangyun Park of Georgia Institute of Technology.

Diffuse ultrasonic waves method setup, data collection and data analysis are being performed cooperatively by Jinyin Zhu, Hongbin Sun, and Hossein Ariannejad of University of Nebraska, Lincoln.

CONTENT

EXECUTIVE SUMMARY	iv
ACKNOWLEDGEMENTS.....	vii
ACRONYMS.....	xiv
1. Introduction	1
1.1 Project Overview	1
1.2 Context	2
1.3 Research Objectives	2
3. Testing Program.....	3
3.1 Concrete Test Specimens	3
3.2 Dimensions and Reinforcing Details.....	4
3.3 Concrete Formulation.....	4
3.4 Steel Confinement Frame	5
3.5 Casting and Curing Conditions.....	7
3.6 Facilities	7
5. Monitoring and Testing Programs	8
5.1 Materials Testing Program	8
5.1.1 Testing Plan.....	8
5.1.2 Compressive Strength Testing.....	9
5.1.3 Elastic Modulus Testing	9
5.1.4 Splitting Tensile Strength Testing	10
5.2 Visual Inspection of Specimens.....	11
5.2.1 Visual Inspection Overview	11
5.2.2 Crack Monitoring	11
5.2.3 Inspection of Material Testing Cylinders.....	15
5.3 Permanent Expansion Monitoring.....	17
5.3.1 Embedded Temperature Sensors	17
5.3.2 Embedded Strain Sensors.....	17
5.3.3 Long-Gauge Fiber-Optic Deformation Sensors	18
5.4 NDE Method – Acoustic Emission (AE) Method.....	19
5.4.1 Test Setup.....	20
5.4.2 Acoustic Emission	21
5.5 NDE Method – Digital Image Correlation (DIC)	22
5.5.1 DIC Overview	22
5.5.2 Pattern Application and Imaging.....	23
5.5.3 Image Analysis.....	24
5.5.4 Pattern Degradation	24
5.6 NDE Method – Nonlinear Ultrasonic (NLU) Rayleigh Surface Waves.....	25
5.6.1 Overview of NLU Method.....	25
5.6.2 NLU Testing on Concrete Specimens.....	26
5.7 NDE Method – Diffuse Ultrasonic Waves (DUW).....	26

5.7.1	Overview of Diffuse Ultrasonic Waves (DUW) Method.....	26
5.7.2	Diffuse Ultrasonic Waves Method Testing on Concrete Specimens.....	27
6.	Results.....	29
6.1	Material Testing.....	29
6.1.1	Compressive Strength.....	29
6.1.2	Elastic Modulus.....	30
6.1.3	Splitting Tensile Strength.....	31
6.2	Strain and Deformation Monitoring.....	32
6.2.1	Early Concrete Age	32
6.2.2	Sensor Correlation.....	33
6.2.3	ASR-Induced Expansion.....	35
6.3	NDE Method – Acoustic Emission (AE)	36
6.3.1	Volumetric Strain Rate	36
6.3.2	Data Filtering	37
6.3.3	Results.....	39
6.3.4	Damage Index	41
6.4	NDE Method – Digital Image Correlation (DIC)	43
6.4.1	Measured Strains	43
6.5	NDE Method – Nonlinear Ultrasonic (NLU) Rayleigh Surface Waves.....	45
6.5.1	Relative Acoustic Nonlinearity Parameter.....	45
6.6	NDE Method – Diffuse Ultrasonic Waves (DUW).....	46
6.6.1	Effect of ASR on Relative Wave Velocity and Temperature Relationship	46
8.	Discussion of Results	49
8.1	Expansion Monitoring – Significance for In-Situ Conditions Assessment	49
8.1.1	Visual Inspection.....	49
8.1.2	Sensors Resilience	49
8.1.3	Expansion Anisotropy.....	50
8.1.4	Effect of Confinement on Material Properties	52
8.2	Discussion of Acoustic Emission NDE.....	54
8.2.1	Advantages and Limitations.....	54
8.2.2	Comparison with Permanent Strain Monitoring Data.....	54
8.3	Discussion of Digital Image Correlation NDE	55
8.3.1	Advantages and Limitations.....	55
8.3.2	Comparison with Permanent Strain Monitoring Data.....	55
8.4	Discussion of Nonlinear Ultrasonic (NLU) Rayleigh Surface Waves	55
8.4.1	Advantages and Limitations.....	55
8.4.2	Comparison with Permanent Strain Monitoring Data.....	56
8.5	Discussion of Diffuse Ultrasonic Waves (DUW)	56
8.5.1	Advantages and Limitations.....	56
8.6	Applications of NDE Methods for Detecting/Assessing ASR in NPP Concrete Structures.....	56
9.	Conclusions and Prospective Work.....	58
10.	References	59

FIGURES

Figure 1: Layout of the three large-scale concrete specimens	3
Figure 2: Large scale mockup dimensions and axis labels (Hayes et al., 2018).....	4
Figure 3: Design of steel confinement frame cross-section (Hayes et al., 2018).....	6
Figure 4: Plan view of steel confinement frame (Hayes et al., 2018).....	6
Figure 5: CASR cylindrical specimen in steel mold	9
Figure 6: Compression and elastic modulus test cylinder after failure	10
Figure 7: Split tensile specimen after failure.....	10
Figure 8: Crack monitoring and marking of unconfined, reactive concrete specimen (1/17/2017).....	11
Figure 9: Comparison of cracking between 12/12/16 (left) and 1/17/17 (right).....	12
Figure 10: Comparison of cracking between 1/17/17 (left) and 5/24/17 (right).....	13
Figure 11: Comparison of cracking between 5/24/17 (left) and 6/28/17 (right) – deterioration of markings is present	13
Figure 12: Digitized crack locations on sides of UASR specimen	14
Figure 13: Typical early crack pattern on unconfined reactive test cylinders	16
Figure 14: Evidence of fracture path through aggregate.....	16
Figure 15: Layout for embedded strain transducers (Hayes et al., 2018).....	18
Figure 16: Layout for fiber optic extensometers (Hayes et al., 2018)	19
Figure 17: AE sensor layout for (a) CASR, (b) UASR, and (c) CTRL	20
Figure 18: AE sensor setup	21
Figure 19: AE acoustic emission	22
Figure 20: Digital Image Correlation (DIC) system and speckle pattern.....	23
Figure 21: White background paint being applied to UASR specimen	23
Figure 22: DIC cameras located above the pattern on the UASR specimen	24
Figure 23: The NLU measurement setup for nonlinear Rayleigh surface waves	26
Figure 24: Test setup for diffuse ultrasonic wave method on concrete specimens	27
Figure 25: Ultrasonic monitoring system and sensors	28
Figure 26: Mean compressive strength of concrete cylinders with increasing age.....	30
Figure 27: Mean elastic modulus of concrete cylinders with increasing age.....	31
Figure 28: Mean splitting tensile strength of concrete cylinders with increasing age.....	32
Figure 29: Early age concrete temperature (Hayes et al., 2018).....	33
Figure 30: Correlation of Z-direction sensors of CASR specimen (Hayes et al., 2018).....	34
Figure 31: Correlation of Z-direction sensors of UASR specimen (Hayes et al., 2018).....	34
Figure 32: Expansion of each specimen in each direction (Hayes et al., 2018).....	35

Figure 33: Volumetric expansion of reactive specimens (Hayes et al., 2018)	36
Figure 34: Volumetric strain and rate	37
Figure 35: Amplitude and CSS versus time	40
Figure 36: Comparison of CSS and expansion	41
Figure 37: b-value	42
Figure 38: Intensity analysis	42
Figure 39: Progression of DIC strain images for strain in X-direction	44
Figure 40: Progression of DIC strain images for strain in Y-direction	44
Figure 41: Summary of measured b values for the CTRL, UASR, and CASR specimens normalized to day 271 CTRL value (Kim et al., 2018)	45
Figure 42: Representative time domain signals for each specimen	47
Figure 43: Relative velocity change as a function of temperature	48
Figure 44: Expansion history of UASR specimen with first cracking observations (Hayes et al., 2018)	49
Figure 45: Z-direction expansion as a function of one-third volumetric expansion (Hayes et al., 2018)	51
Figure 46: X-direction expansion as a function of one-third volumetric expansion (Hayes et al., 2018)	51
Figure 47: Change in relative compressive strength with ASR expansion (Hayes et al., 2018)	53
Figure 48: Change in relative elastic modulus with ASR expansion (Hayes et al., 2018)	53

TABLES

Table 1: Descriptions of cylinder types	8
Table 2: Testing dates for concrete material testing	8
Table 3: Types and quantities of sensors for all specimens (Hayes et al., 2018)	17
Table 4: Mean and standard deviation (SD) compressive strength of concrete cylinders	29
Table 5: Average and standard deviation of modulus of elasticity of concrete cylinders	30
Table 6: Average split tensile strength of concrete cylinders	31
Table 7: Duration amplitude rejection limits	39
Table 8: DIC measured surface strains and facets	43
Table 9: Summary of measured expansion and b: CTRL specimen (Kim et al., 2018)	46
Table 10: Summary of measured expansion and b: CASR specimen (Kim et al., 2018)	46
Table 11: Summary of measured expansion and b: UASR specimen (Kim et al., 2018)	46

ACRONYMS

AE – acoustic emission
ASR – alkali-silica reaction
CASR – confined alkali-silica reaction specimen
CTRL – unreactive, control specimen
DIC – digital image correlation
DUW – diffuse ultrasonic wave
GT – Georgia Institute of Technology
NDE – nondestructive evaluation
NLU – nonlinear ultrasonic
NPP – nuclear power plant
SD – standard deviation
UASR – unconfined alkali-silica reaction specimen
UNL – University of Nebraska Lincoln
USC – University of South Carolina
UTK – University of Tennessee Knoxville
VU – Vanderbilt University

1. Introduction

1.1 Project Overview

Concrete structures, such as nuclear power plant (NPP) structures, are designed to withstand potential durability, serviceability, and safety issues. Unfortunately, Alkali-Silica Reaction (ASR) is a major degradation mechanism of concrete that has often created a need for aging management and repair for many of these infrastructures. Several cases of ASR in NPP structures have been disclosed in Japan, Canada at Gentilly 2 NPP, and recently in the United States. Because of the deleterious effects of ASR in nuclear concrete structures, a need is present in identifying the degree at which ASR affects NPP structures which are commonly unreinforced in the thickness direction. With NPP concrete wall structures typically having a relatively large thickness, shear strength is achieved solely by the shear capacity of the concrete. Thus, these walls are typically designed unreinforced for shear stresses as allowed by ACI 318 (ACI Committee, 2014). Due to the existence of steel reinforcement within the concrete structure designed for flexural and axial loads, the lateral in-plane directions of the structure are typically confined against expansion. This confinement in the in-plane directions deters expansion due to ASR; additionally, the lack of reinforcement in the thickness direction of the structure allows for unconfined ASR expansion. The effects of these differences in confinement conditions in the development of ASR swelling and micro-cracking are important in understanding the effect of ASR expansion on the deterioration of mechanical properties of the concrete for these particular structures. At the macro-scale, the development of the ASR-induced concrete expansion is conditional to the possibility of free expansion: compression in one or two directions causes a preferential expansion in the free direction. This research endeavor aims to extend the existing body of knowledge on the formation of ASR damage in stress-confined nuclear structures and its effect on the structural resistance of ASR-affected reinforced concrete members.

Although the residual shear capacity of the ASR-affected stress-confined concrete is one of the research objectives, the deterioration of several mechanical properties of the concrete as a function of ASR expansion is also being investigated to develop and improve reliable condition assessment methodologies including ASR models. The characterization of mechanical properties as a function of the stress-confined ASR expansion will be used to validate and improve models to more accurately predict the effects of confinement on the development of ASR damage in nuclear structures.

To achieve these objectives, three concrete specimens were cast and placed within a controlled environmental chamber. The concrete used for these specimens was designed to experience sufficient ASR expansion. Each of the three specimens is heavily instrumented with multiple types of sensors measuring deformation, strain, temperature. These specimens are being subjected to ASR for a period of two years. After the period of allowed reaction, the specimens will be mechanically tested to observe the effects of ASR on their shear capacity.

1.2 Context

Due to the recent observations of ASR at the Seabrook Station nuclear power plant, demand for a better understanding of the mechanisms and effects of ASR in nuclear power plant structures has increased. Several studies have investigated the effects of ASR on the mechanical properties of concrete. Some studies have specifically investigated the effects of ASR on the shear strength of reinforced beams that are reinforced with stirrups as shear reinforcement (*Seabrook Station Response to NRC letter to NextEra Energy Seabrook CAL No. 1-2012-002*, 2013) (Saouma, Hariri-Ardebili, Le Pape, & Balaji, 2016). However, in a typical nuclear power plant thick wall structure, shear reinforcement is not required for structural strength as allowed by ACI 318 (ACI Committee, 2014) due to the significant depth of concrete contributing to the shear resistance of the structural element. With the planar section of the wall being heavily reinforced for the predicted loads, this can lead to a severe case of anisotropic expansion due to ASR. As ASR attempts to expand in the planar directions of the wall, the expansion is resisted by the steel reinforcement. This anisotropy will drive the majority of the expansion in the unreinforced direction, leading to significantly different conditions as opposed to the concrete beam with both longitudinal and shear steel reinforcement. Experimental data on the effects of ASR in the specific case of a thick walled concrete structures with no shear reinforcement are necessary to quantify the effect of ASR damage on typical nuclear power plant structural elements.

1.3 Research Objectives

The primary objective of this research is to quantify the effect of ASR on the shear strength of a typical nuclear power plant thick-walled concrete structure. This objective will be accomplished by allowing the concrete specimens to be exposed to accelerated ASR for a period of approximately two years. During this expansion period, each specimen is continuously and closely observed by several monitoring systems. After which, each specimen will be sawed into beams and tested for shear capacity. The effects of the differing boundary conditions in combination with ASR will be observed and quantified.

The main feature of this experiment as opposed to previous investigations in the literature is the difference in specific boundary conditions as well as the geometry of the specimens. To accurately assess the development and effects of ASR in typical nuclear power plant concrete structures, a specimen must be observed that closely mimics the boundary conditions present in such a structural element. Thus, the specimens used in this study have been designed with no shear reinforcement. The absence of shear reinforcement can significantly alter the development of expansion due to ASR within concrete leading to a less random pattern of cracking primarily creating expansion in the unreinforced direction. The more uniform crack pattern will affect the mechanical properties of concrete differently as opposed to random crack patterns of unconfined or uniformly confined concrete specimens.

3. Testing Program

3.1 Concrete Test Specimens

A structural specimen detail was designed to closely resemble a typical nuclear power plant containment structure to investigate the effects of ASR on thick-walled concrete structures with no shear reinforcement (Hayes et al., 2018). Specimens were designed with a thickness of 1.0 meter and reinforced only in the plane of the wall with two elevations of intersecting large steel reinforcement leaving the thickness of the wall entirely unreinforced.

Three unique specimens were conceptualized and constructed. The layout of the three specimens is shown in *Figure 1*. The first specimen, referred to as the confined ASR specimen (CASR), was surrounded by a rigid steel frame constructed to simulate the additional confinement by surrounding concrete that would be present in a nuclear power plant (NPP) containment structure. This steel frame confines the concrete specimen against expansion in the plane of the wall, forcing a preferred direction of expansion through the thickness.

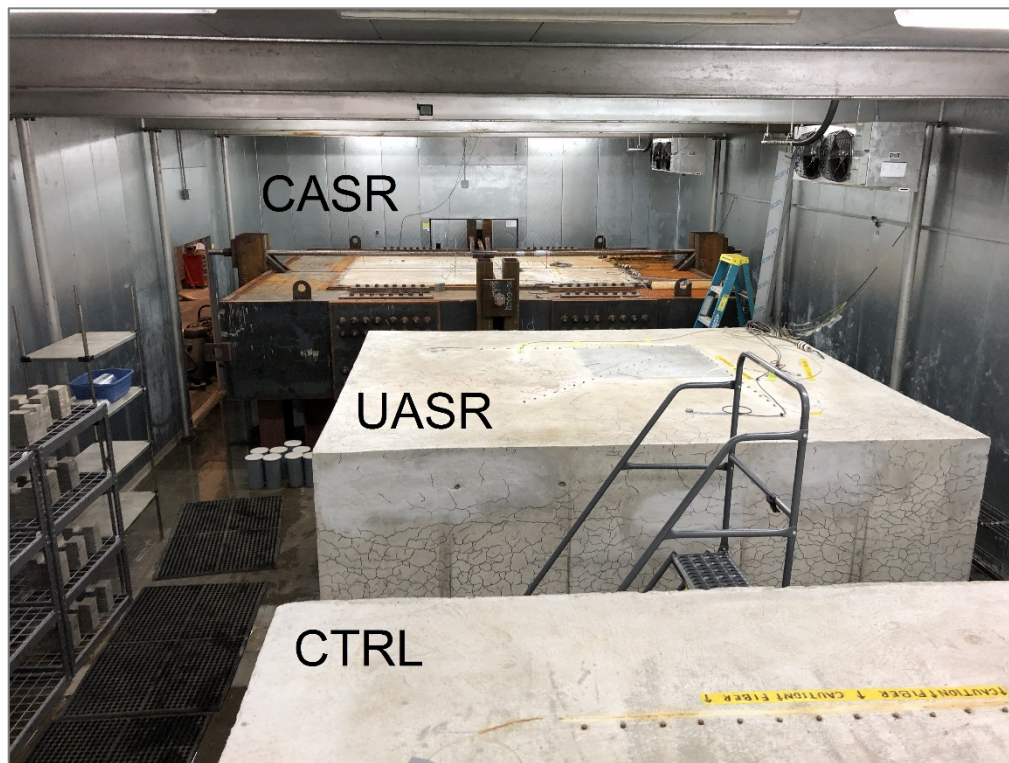


Figure 1: Layout of the three large-scale concrete specimens

The second specimen, referred to as the unconfined ASR specimen (UASR), with identical mix design and steel reinforcement detail was designed and constructed with no surrounding steel frame. Thus, this specimen is unrestrained by exterior boundary conditions but still partially restrained against expansion in the plane of the wall by the steel reinforcing bars.

The third specimen, referred to as the control specimen (CTRL), with identical steel reinforcement was designed and constructed with a change to the mixture design to minimize the potential for expansion from ASR. Sodium hydroxide (NaOH), used to promote the development of ASR in the CASR and UASR specimens, was not used in the mix design for the CTRL specimen. Instead, a lithium nitrate

admixture was added to mitigate against the alkalis contributed by the cement. No ASR expansion was observed in this specimen.

For the sake of practicality, the specimens were cast horizontally. Hence, the actual through-wall thickness corresponds to the vertical direction (Z).

3.2 Dimensions and Reinforcing Details

Specimen dimensions were selected to represent the scale of a typical NPP containment structure. The through-thickness dimensions (Z-direction) is 1.0 meter. The dimensions within the plane of the wall were selected accordingly at 3.5 meters and 3.0 meters for the X-direction and Y-direction respectively (Hayes et al., 2018). These dimensions are shown in *Figure 2*.

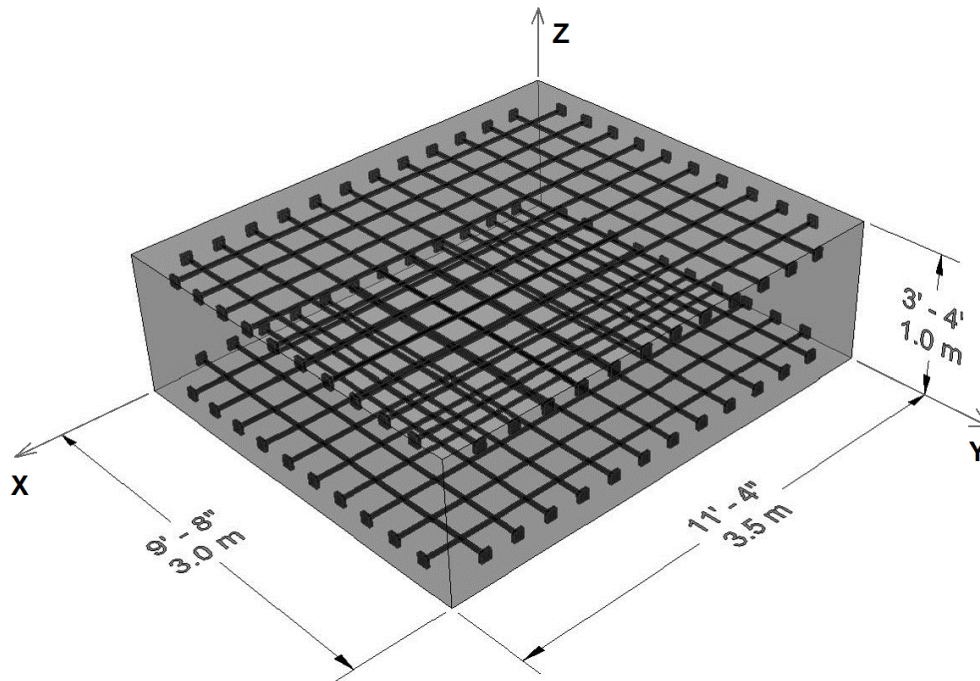


Figure 2: Large scale mockup dimensions and axis labels (Hayes et al., 2018)

The reinforcement layout for the specimens was also selected to most closely resemble that of a NPP structure. The reinforcement layout consists of US #11 Gr. 60 (yield stress of 415 MPa) reinforcing steel bars with a nominal diameter of 35.81 mm spaced at 25.4 cm on-center resulting in two elevations of reinforcing bars embedded in the concrete specimens with 7.62 cm of concrete cover. The reinforcement layout results in only the plane directions of the wall reinforced at a ratio of approximately 0.68%. The reinforcing bars were installed with square heads (10.2 cm x 10.2 cm x 2.5 cm) made of steel plate to achieve full development lengths within a shorter distance inside the specimen.

The specimens are elevated above the floor by four steel columns capped with 45.7 cm x 45.7 cm steel plates. The contact at these supports is simply concrete-to-steel.

3.3 Concrete Formulation

A trial study was performed to identify the ideal mix designs. Two mixtures were developed: (1) a reactive mixture that exhibited free expansion equal to roughly 0.15% per year, and (2) a mitigated control mixture that does not expand (Hayes et al., 2018). Both mixtures utilize the same highly reactive coarse aggregate, relatively non-reactive fine aggregate, and Portland cement. Sodium hydroxide was

added to the reactive mixture, and lithium nitrate admixture was added to the control mixture. A high-range water-reducing admixture and hydration stabilizer were added maintain consistent slump values between 15 and 20 cm and offset the effects of warm ambient temperatures that would otherwise accelerate setting of the concrete during placement. A large quantity of mixing water was replaced with ice in order to reduce placement temperature to avoid delayed ettringite formation.

3.4 Steel Confinement Frame

In order to simulate the range of structural boundary conditions present in a large structure such as a NPP containment building, two cases were considered: (1) a reinforced concrete specimen unconstrained laterally, and (2) a similar specimen encased in a rigid steel frame, restraining lateral deformation in the plane of the reinforcement and allowing unrestrained expansion through the specimen thickness (Hayes et al., 2018).

To provide sufficient rigidity, the confinement frame was designed for maximum stiffness within the allotted space. A steel plate girder cross-section was designed consisting of two 76 mm flanges and three 51 mm webs as shown in *Figure 3*. Because of limited lifting capabilities, the frame was designed as four sections joined by slip-critical bolted connections, each consisting of twelve splice plates and 144 steel bolts. The connected elements of the steel frame confining the specimen is demonstrated in *Figure 4*. The cross-section and connections were designed for a maximum pressure of 8 MPa at the steel frame-concrete interface and a corresponding maximum deflection of 2.5 mm. In order to reduce frictional effects between the steel frame and concrete specimen, a single 1.5 mm-thick layer of high-density polyethylene (HDPE) was placed at the interface.

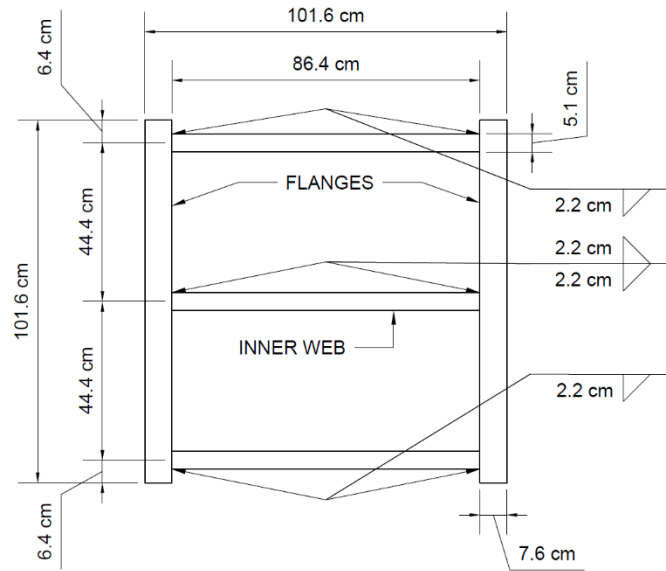


Figure 3: Design of steel confinement frame cross-section (Hayes et al., 2018)

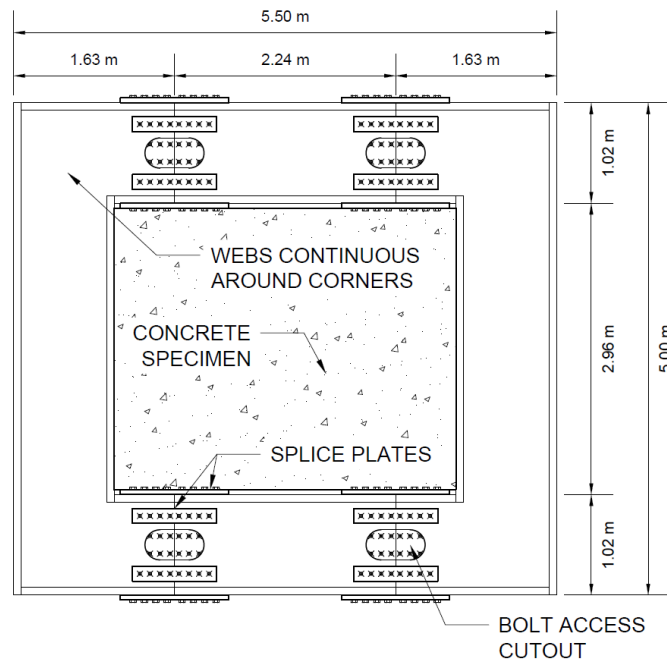


Figure 4: Plan view of steel confinement frame (Hayes et al., 2018)

3.5 Casting and Curing Conditions

Casting took place on July 23, 2016. In an attempt to mitigate potential damage sources other than ASR (e.g. thermal cracking), the formwork was insulated prior to the concrete placement with rigid foam insulation. Additional sheathing was installed on top of the specimens shortly after initial set and final finishing of the top surfaces.

To avoid any possible detrimental delayed ettringite formation (DEF)-induced expansion, the temperature within the concrete specimens during early-age curing was maintained below 70 °C by substituting 70% of mixing water with ice.

All formwork was removed on August 4, 2016. After final finishing and setting of the concrete, each exposed surface of the specimens was sprayed with a curing compound and then covered with a layer of wet burlap and plastic sheeting to minimize any moisture loss and mitigate early-drying-induced cracking. The burlap was periodically moistened until full operation of the environmental chamber.

3.6 Facilities

The specimens were exposed to accelerated curing conditions within an environmental chamber designed for temperature and humidity control of 38 ± 1 °C and $95 \pm 5\%$ relative humidity (RH). In order to maintain the temperature and RH during operation, a heating system consisting of both heating evaporators and heating units accommodated by air circulators was designed.

The environmental chamber was delivered as panels consisting of embossed steel filled with foam insulation. Each panel has a set of locks to secure adjacent panels together. The floor connection is sealed by a vinyl sealer underneath the wall panels to the concrete floor of the high bay laboratory. To allow the construction of the three specimens, the environmental chamber was built around the specimens a few weeks after casting.

A full power up of the heating system was completed on August 17, 2016 to test the operation of the heating and misting system as well as the lighting system. After confirmation of the systems working order, the system was powered down to finalize all connections and prepare the chamber for full-time operation. All concrete specimens were uncovered at this time. The chamber measures approximately 16.2 m long, 7.3 m wide, and 3.7 m high. This volume allowed all three reinforced concrete specimens and all concrete companion cylinders for material testing to be contained within the same environment.

The chamber was initialized for full operation on August 19, 2016 (concrete age of 26 days). The chamber was operated uninterrupted, except for periodic inspections, at the specified environmental conditions. The relatively high temperature and moisture conditions constitute a working safety hazard. Hence, the chamber is periodically shutdown during inspection of the specimens at an average frequency of two days per month. During shutdowns, the average temperature and RH are about 25 °C and 60% (transient of about 4 hours). After the shutdown period, the chamber is restarted; the temperature and humidity return to the original set points within 6 hours. The time period of chamber shutdowns is small (less than 5% of overall monitoring time). The change in temperature shutdown is accompanied by thermal strains of the concrete; however, because continuity is observed in the measured strains before and after temperature changes, the chamber shutdowns had no effect on the concrete confinement provided by the steel frame.

5. Monitoring and Testing Programs

5.1 Materials Testing Program

5.1.1 Testing Plan

To characterize the effect of ASR on the mechanical properties of the concrete, a material testing program was developed to accompany the testing of the large-scale mockups. The large-scale mockups were labeled as confined reactive specimen (CASR), unconfined reactive specimen (UASR), and unreactive control specimen (CTRL) as discussed in Chapter 1 and noted in **Table 1**. Concrete compressive strength, elastic modulus, and split tensile strength for each type of large scale mockup specimen were tested at the dates listed in **Table 2**.

Table 1: Descriptions of cylinder types

Cylinder Type	Description
CASR	Confined ASR specimen
UASR	Unconfined ASR specimen
CTRL	Control non-expansive specimen

Table 2: Testing dates for concrete material testing

Age (days)	Age (years)	Test Date
0	0.00	7/23/2016
7	0.02	7/29/2016
28	0.08	8/19/2016
91	0.25	10/21/2016
183	0.50	1/23/2017
274	0.75	4/24/2017
365	1.00	7/24/2017
548	1.50	1/22/2018
730	2.00	7/23/2018

At each test date, five cylinders of each type were tested; three were tested for compressive strength and elastic modulus simultaneously, and two were tested for split tensile strength. At each test date, three 150 mm diameter by 300 mm height cylinders were tested for elastic modulus and compressive strength for each type of large-scale concrete specimen, and two cylinders of the same dimensions were tested for split tensile strength. CASR material testing specimens were cast utilizing the same concrete used to prepare the confined, reactive large-scale mockup specimen. The specimens were cast in steel molds and remained in the molds to simulate the confined boundary condition as shown in **Figure 5**. UASR material testing cylinders were cast utilizing the same concrete used to prepare the unconfined, reactive large-scale concrete specimen. These specimens were cast in disposable plastic molds and removed from the molds 48 hours after pouring leaving the specimens free to expand due to ASR. CTRL material testing cylinders were cast utilizing the same concrete used to prepare the control, non-expansive large-scale concrete specimen. These specimens were also cast in plastic molds and removed from the molds a few days after pouring.



Figure 5: CASR cylindrical specimen in steel mold

5.1.2 Compressive Strength Testing

The concrete was tested for compressive strength in accordance with ASTM C39 (I. ASTM, 2016). Compression tests were conducted with a Gilson MC-500PR Concrete Compression Testing Machine. Compressive strength testing was conducted simultaneously with elastic modulus testing. It is well known in the literature that the compressive strength decreases as damage due to the reaction increases at the micro-structural level (Marzouk & Langdon, 2003). Many investigations have reported that loss of compressive strength can be as high as 60% in research conditions ultimately depending on the type of aggregate, concrete mix design, and exposure conditions (R. Swamy, 1994).

5.1.3 Elastic Modulus Testing

The concrete was tested for static modulus of elasticity in accordance with ASTM C469 (I. ASTM, 2014). Modulus of elasticity tests were conducted with a Gilson MC-500PR Concrete Compression Testing Machine and Admet C-1217DAE Controller with Compressometer as shown in **Figure 6**. Elastic modulus testing was conducted simultaneously with compressive strength testing. For the first cylinder specimen of each set of three designated for testing compressive strength and modulus of elasticity, the compressometer was installed and the cylinder was tested to failure. For the second and third specimens, the compressometer was installed to the cylinder and three iterations of tests were performed. For the first and second cycles, the cylinders were loaded to approximately 40% of the ultimate compressive strength of the first specimen and deformation of the cylinder was recorded every one-thirtieth of a second. For the third cycle, the cylinder was tested until failure with the compressometer still attached, and deformation was recorded. With this information, the static modulus of elasticity for each cycle was calculated and an average value amongst all cycles was reported for each test age.



Figure 6: Compression and elastic modulus test cylinder after failure

5.1.4 Splitting Tensile Strength Testing

The concrete was tested for split tensile strength in accordance with ASTM C496 (I. ASTM, 2004). Split tensile tests were conducted with an Instron Universal Testing Machine 5593-F1-G1 and testing rig with supplementary bearing bar as shown in *Figure 7*. Specimens were placed in the testing rig and properly aligned. The specimens were loaded at the rate specified by the standard procedure until failure of the specimen.

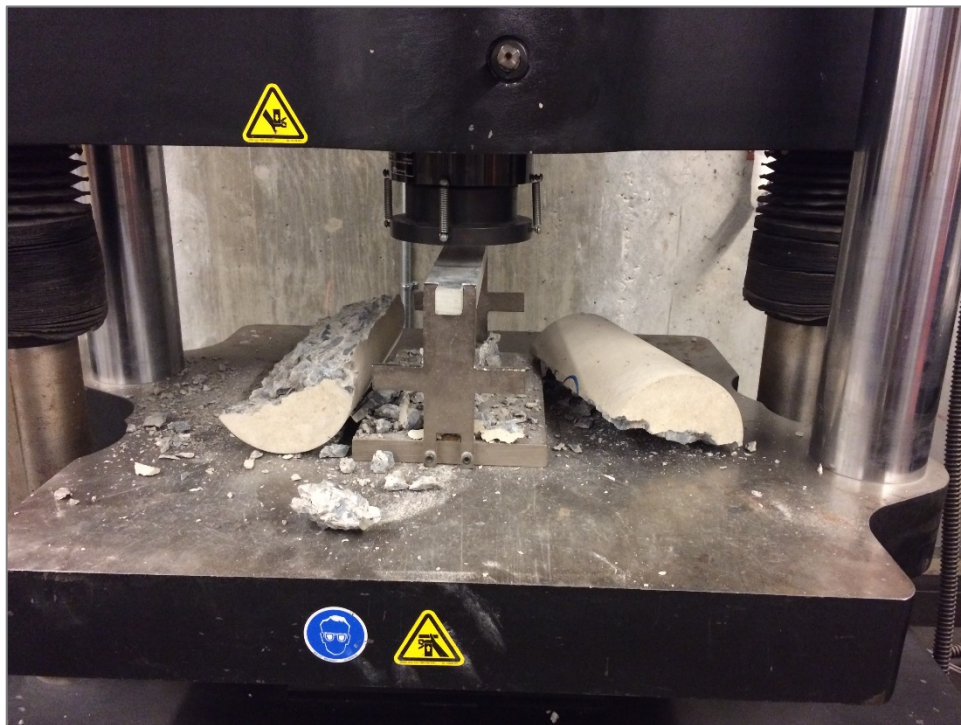


Figure 7: Split tensile specimen after failure

5.2 Visual Inspection of Specimens

5.2.1 Visual Inspection Overview

Cracks in the concrete were first noticed 141 days after the concrete pour (12/12/2016). At that point, the unconfined reactive specimen was thoroughly inspected for cracks. The cracks were marked for reference. Cracks were marked periodically during the expansion period. **Figure 8** shows the unconfined reactive specimen with marked cracks.



Figure 8: Crack monitoring and marking of unconfined, reactive concrete specimen (1/17/2017)

5.2.2 Crack Monitoring

The unconfined, reactive specimen was divided into panels for crack monitoring. The specimen is thoroughly inspected for cracks and marked periodically. Photos of marked cracks are compared for crack progression to visualize the progression of cracking on the surface. Cracks on the side of the UASR specimen were first observed in December of 2016. **Figure 9** shows side-by-side images of marked cracks at December 12, 2016 and January 17, 2017. It is worth noting that some small defects (voids, honeycombing) on the sides of the UASR specimen were observed after removal of the formwork. These defects were corrected with standard patch concrete in an attempt to be able to better identify cracks on the surfaces.



Figure 9: Comparison of cracking between 12/12/16 (left) and 1/17/17 (right)

Marking of cracks was conducted at chamber deactivations. As shown in **Figure 10**, the number of visible cracks has significantly increased since January 2017. Multiple colors were used to mark cracks to distinguish between dates. Ignoring the deterioration of markings, comparisons of images in the later consecutive months indicate very little change in the number of cracks as shown in **Figure 11**. Between 5/24/17 and 6/28/17, small amount of additional cracks were found with majority of those being bifurcations of existing cracks. Due to deterioration of crack markings in colors other than black, all cracks were remarked with black permanent marker in February 2018.

Cracks on the top surface of the UASR specimen were first observed in June of 2017. Starting from July 2017, cracks on the top surface of the UASR specimen are marked at each chamber deactivation. To date, the degree of cracking on the top surface is much less than that on the side surfaces of the UASR specimen. Additionally, cracks were observed nearly six months earlier on the specimen sides in comparison to the top surface. It is worth noting that at even after 2 years of accelerated testing, there are no visible cracks on the top surface of the confined specimen (CASR). The sides of the CASR specimens could not be inspected because of the steel confinement frame.

Figure 12 shows the digitized surfaces of the UASR with all cracks marked as of February 2018. There were very little changes in the number of observable cracks on the surfaces between February 2018 and July 2018.



Figure 10: Comparison of cracking between 1/17/17 (left) and 5/24/17 (right)



Figure 11: Comparison of cracking between 5/24/17 (left) and 6/28/17 (right) – deterioration of markings is present

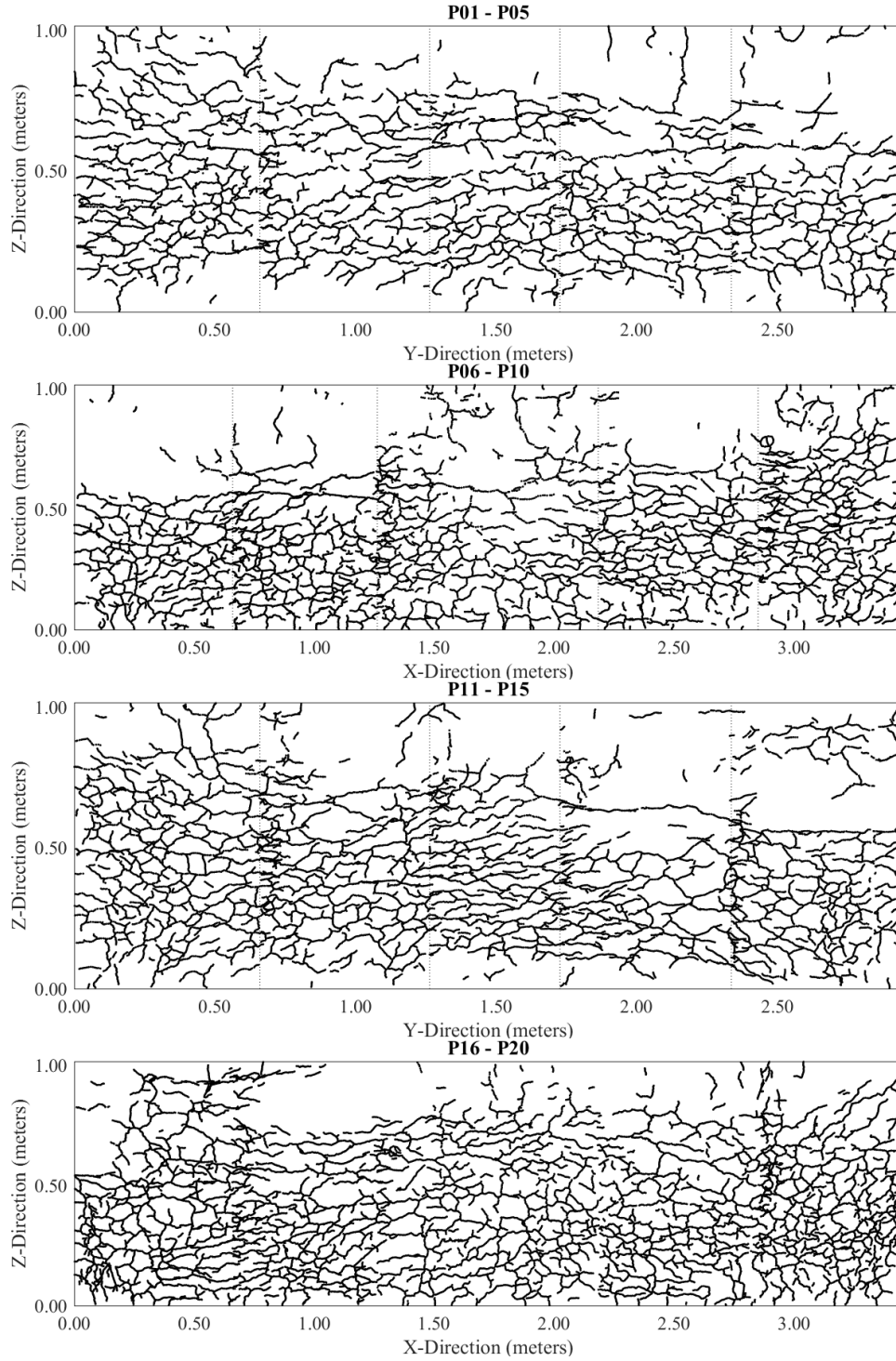


Figure 12: Digitized crack locations on sides of UASR specimen

5.2.3 Inspection of Material Testing Cylinders

The concrete cylinders used for material testing are also showing signs of ASR damage. At each testing date, the concrete cylinders are closely inspected before and after testing. The unconfined, reactive specimens are now showing small cracks on the surface. The crack pattern on these unconfined specimens appears largely random as seen in **Figure 13** without a single dominant direction which is expected due to the lack of confinement. The top and bottom surfaces of the unconfined material testing specimens also show some cracking. However, cracking on the surfaces of the confined material testing specimens after remove from molds do not show any visible cracks other than at the connection of the mold.

The split tensile specimens were observed after failure. It was noticed that some aggregates had been fractured during the test. **Figure 14** shows evidence of fracture through aggregate. The fracture path through the aggregate could indicate a weak aggregate which could also explain the reason behind the rapid rate of ASR expansion. A weak aggregate would easily crack due to ASR gel expansion within the aggregate. As the aggregate fractures due to expansion within the concrete, more surface area of the aggregate can become exposed to the alkaline pore solution leading to an increased amount of available amorphous silica for the alkaline pore solution to react with.



Figure 13: Typical early crack pattern on unconfined reactive test cylinders



Figure 14: Evidence of fracture path through aggregate

5.3 Permanent Expansion Monitoring

The concrete specimens were heavily instrumented to monitor local strain, structural deformations, and temperature within the bulk and on the surfaces of the specimens as the ASR progressed. In total, three main different types of sensors were utilized as shown in **Table 3**. These sensors were connected to automated data acquisition systems. Data was automatically collected from each of these sensors once per hour for the entire test duration.

Table 3: Types and quantities of sensors for all specimens (Hayes et al., 2018)

Sensor	Quantity
<i>Temperature:</i>	
Thermocouple	12
<i>Deformation/Strain:</i>	
Strain transducer	64
Long-gauge FO extensometer	12

5.3.1 Embedded Temperature Sensors

Temperature monitoring is required to: (1) assess the (absence of) risk for DEF, (2) verify the uniformity of temperature within specimens, and (3) provide potential thermal correction factors for additional measurements taken during temperature transients such as at early-age and during environmental chamber shutdowns. Monitoring of temperature was initiated shortly before concrete placement using thermocouples that were built into the strain transducers. A total of four thermocouples were placed in each specimen in such a way that two temperature gradients could be obtained. A vertical line of three thermocouples were installed near the center mass of the specimen in order to measure the vertical (Z-direction) temperature gradient with two sensors installed 25 cm above and below the bottom and top surfaces of the specimens and one thermocouple installed mid-depth within the specimen. The fourth thermocouple within each specimen was placed at mid-depth near a corner to measure the X and Y plane temperature gradient.

5.3.2 Embedded Strain Sensors

A total of 64 100 mm-gauge strain transducers (KM-100B or KM-100BT from Tokyo Sokki Kenkyujo) were embedded in the concrete specimens. The transducers were installed using nylon cable ties to a support structure of 3 mm-diameter smooth steel bars installed between the two layers of steel reinforcement prior to concrete placement. These sensors have shown remarkable durability in previous research including ASR studies (Bracci, Gardoni, Eck, & Trejo, 2012; Herrmann et al., 2008). The strain transducers were arranged within the specimens as shown in **Figure 15**. The placement of the strain transducers was designed to: (1) measure strains in all directions, (2) evaluate strains special variability by increasing the density of sensors in a single quadrant, and (3) limit possible interactions with NDE based on acoustic wave propagation techniques by reducing the density of sensors in the opposite quadrant.

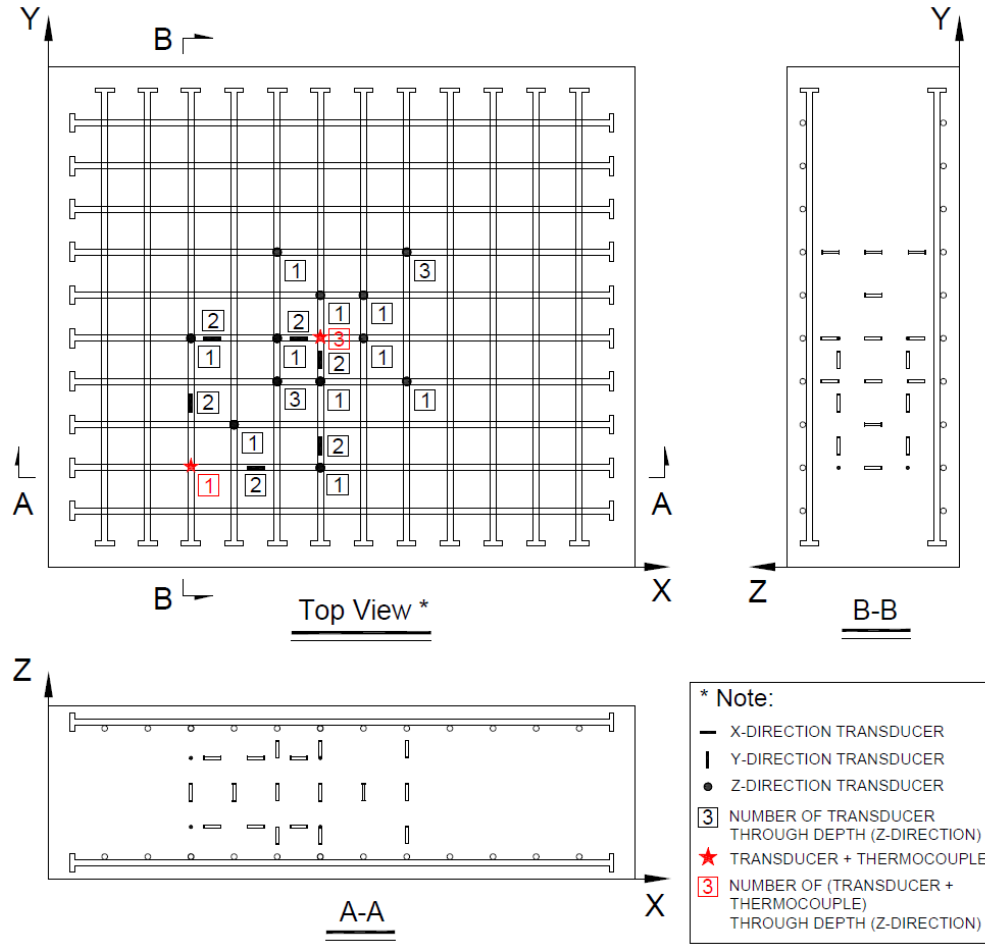


Figure 15: Layout for embedded strain transducers (Hayes et al., 2018)

5.3.3 Long-Gauge Fiber-Optic Deformation Sensors

In addition to the local strain measurement, the overall structural expansion was also monitored for each principal direction of each specimen. High precision (≈ 2 mm) and accuracy fiber-optic (FO) extensometers (SOFO standard deformation sensor from SMARTTEC/Roctest) (Glisic, Hubbell, Sigurdardottir, & Yao, 2013; Inaudi, 1997) were placed at the bottom surface of the specimens and inside the concrete, for the horizontal and vertical deformation measurements, respectively. The vertical FO extensometers, of 0.8 m gauge length, measure the deformation between the top and bottom reinforcement layers and were attached to a 3 mm-diameter steel smooth bar with nylon cable ties before concrete placement. The 1.5 m-gauge length horizontal FO extensometers were placed at the bottom surface of the specimens to allow access to the top surface for NDE. The sensors ends are supported by angle-plates, anchored 7.6 cm deep in the concrete, i.e. reaching the plane of reinforcement. The layout of extensometers is similar for both the restrained and unrestrained specimens as shown in **Figure 16**.

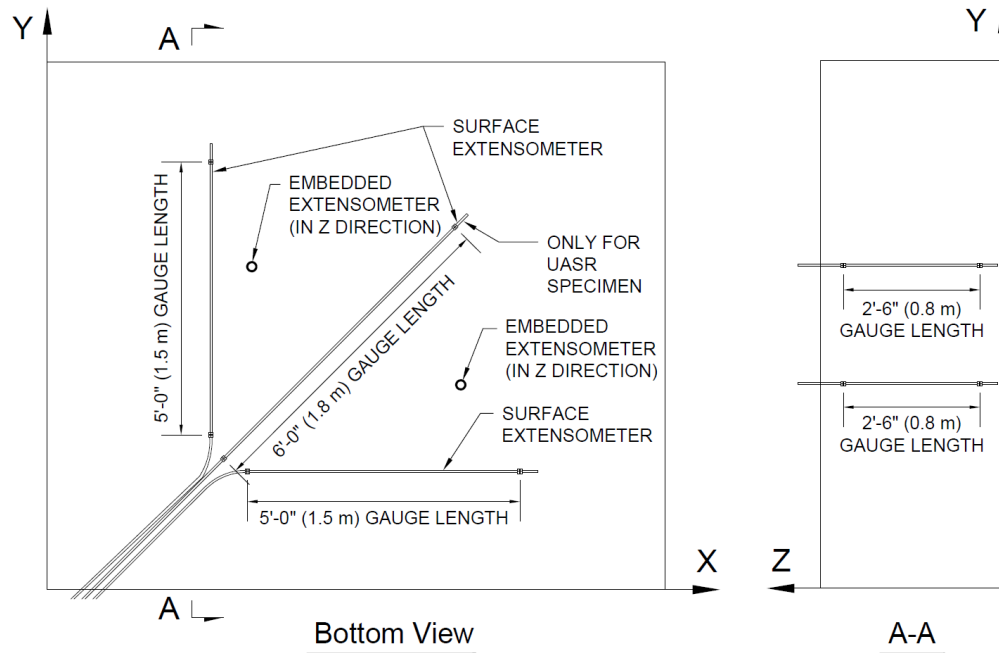


Figure 16: Layout for fiber optic extensometers (Hayes et al., 2018)

5.4 NDE Method – Acoustic Emission (AE) Method

Acoustic emission (AE) is one of the nondestructive methods that has recently been utilized in damage evaluation of concrete structures with alkali-silica reactive aggregates (Abdelrahman et al., 2015; Farnam, Geiker, Bentz, & Weiss, 2015; Lokajíček, Příkryl, Šachlová, & Kuchařová, 2017; Weise, 2012). Acoustic emission consists of elastic transient stress waves that are emitted by the sudden release of energy in a material due to crack formation. These stress waves are transmitted to the electric signals through piezoelectric sensors and then recorded continuously (Anay, Soltangharai, Assi, DeVol, & Ziehl, 2018). This method has some advantages over others. For instance, AE is a passive method, which does not need any excitation for recording data. Therefore, structures can be monitored continuously. This is significant, especially for concrete structures affected by ASR, since ASR is a long-term reaction. Moreover, due to the high sensitivity of AE sensors, internal primary ASR damage can be detected and analyzed before reaching the surface. Contrary to coring, AE data is able to represent the entire condition of the structure, if sensors are arranged appropriately. In addition, the location of damage can be determined by using different algorithm (Ge, 2003; Kobayashi & Shiotani, 2016; Maochen, 2003). In nuclear power plant structures, there is usually a restriction to accessing both sides of the structure. This limits the use of some methods such as ultrasonic measurement. On the other hand, AE data acquisition is possible if only one surface of the structure is available. There are various types of AE data acquisition systems, associated software, and sensors with different applications, which are commercially available. In spite of these advantages, there are some drawbacks that are associated with AE. For instance, AE data is usually contaminated by non-relevant data due to mechanical and electrical noises, which requires filters before analyzing. Filtering and processing AE data is challenging and time-consuming. In addition, for defining a structural damage index, correlation to mechanical properties or expansion strain is required. For the accurate source location in a large-scale structure, the number and arrangement of sensors are essential factors. Furthermore, the surface sensor attachment requires frequent inspection, especially in harsh environmental conditions. AE instrumentations, including data acquisition, cables, sensors, filters, and preamplifiers, are expensive.

Researchers (Lokajiček et al., 2017) evaluated the effect of ASR on mortar bars using AE, ultrasonic sounding, standard expansion measurement, and scanning electron microscopy (SEM). It was shown that AE and ultrasonic sounding were more sensitive to the early ASR damage formation than standard dilation measurement. Researchers (Farnam et al., 2015) also evaluated AE waveforms during ASR test and compared them with the results from wedge splitting test. It was illustrated that the crack formation in aggregates had a higher frequency range than cracks in cement matrix and interfacial transition zone (ITZ). Researchers (Abdelrahman et al., 2015) additionally assessed the effect of ASR on concrete prisms using AE, expansion measurement, and petrographic analysis. A linear correlation was observed between AE data, expansion readings, and petrography damage rating index (DRI).

In this study, AE was utilized to evaluate the ASR effect on the degradation of large-scale reinforced concrete structures. The specimens were continuously monitored by AE and embedded strain gauges. The results illustrated a correlation between volumetric strain and AE data.

5.4.1 Test Setup

Seven acoustic emission sensors were utilized in each of the confined and unconfined specimens (reactive specimens) as shown in **Figure 17**. Two sensors were employed for the CTRL specimen. Three broadband sensors (operating frequency range of 100 - 800 kHz) with an internal low-power 26 dB preamplifiers were installed inside the reinforcement cages before concrete casting for reactive specimens, and one sensor was installed for the control specimen (**Figure 18 a**). Four resonant sensors (operating frequency range of 35 – 100 kHz) each containing an internal 40 dB preamplifier, were attached at the bottom of the reactive specimens and one sensor was attached to the control specimen (**Figure 18**). The resonant sensors were attached with epoxy on the surface of the concrete and fixed by holders as shown in **Figure 18 b**. Internal and external sensors are referred to as broadband and resonant sensors, respectively in this report. The holders were made using stainless steel, and polyurethane pads were attached between concrete and the holders to avoid any potential corrosion in the holders. A 16-channel Sensor Highway II (SHII), manufactured by MISTRAS Group, Inc. (Princeton Junction, New Jersey), was utilized as a data acquisition system. The sensitivity of external sensors was checked by applying Hsu-Nielsen sources (Hsu, 1981).

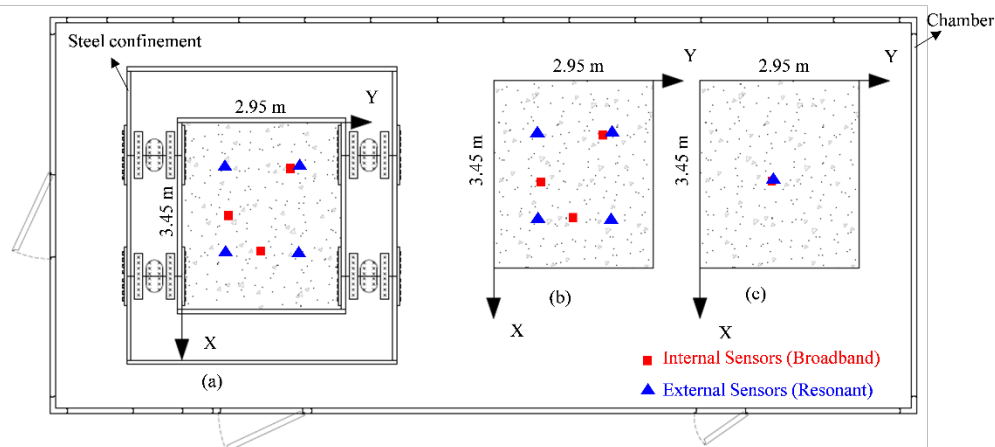


Figure 17: AE sensor layout for (a) CASR, (b) UASR, and (c) CTRL

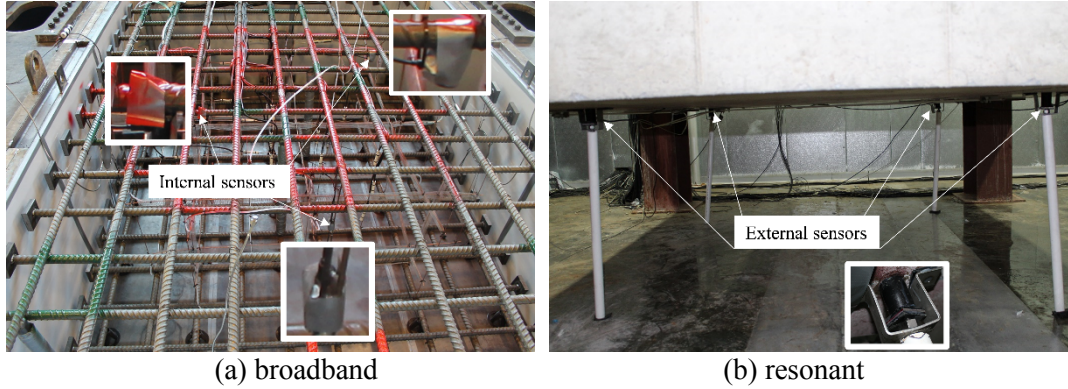
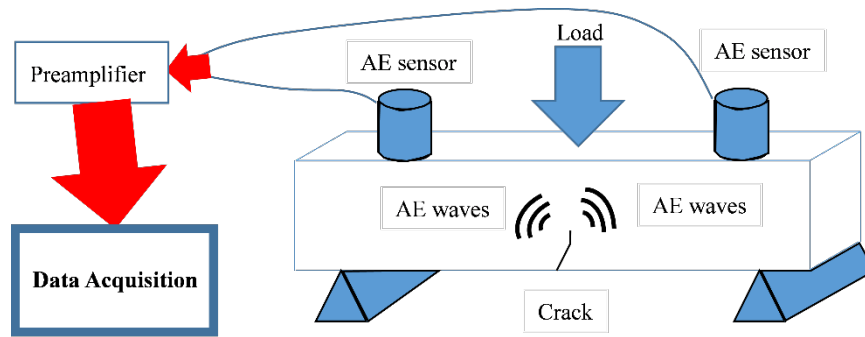


Figure 18: AE sensor setup

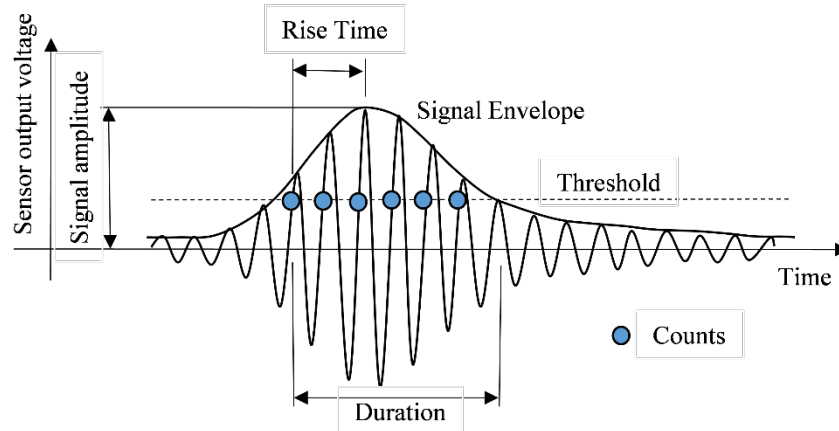
5.4.2 Acoustic Emission

A research team from the University of South Carolina was invited to perform acoustic emission monitoring on the large-scale specimens. Acoustic emission refers to the phenomena whereby elastic waves are emitted by a sudden release of energy due to cracking or damage formation in materials (E. ASTM, 2006; Grosse & Ohtsu, 2008). Elastic stress waves travel through the material to the surface and are transferred into electrical signals by piezoelectric sensors. The signals received are weak; therefore, they must be amplified by either internal or external preamplifiers before being recorded. The schematic AE phenomenon is presented in **Figure 19 a**. Stress waves are continuously recorded through the AE data acquisition system and saved as discrete signals (hits). The signals are recorded when their amplitudes are more than a predefined threshold. Then they are saved based on waveform setup parameters in the data acquisition, including pre-trigger time, peak definition time (PDT), hit definition time (HDT), and hit lockout time (HLT). Pre-trigger time is the period required for data acquisition to save a signal prior to threshold intersection, which was set to 256 micro-second. HDT is the time for terminating the measurement of the waveform, which was set to 400 micro-second. HLT is the time defined at the end of a signal for neglecting any reflected signal that exceeds the threshold, which was set to 200 micro-second. PDT is the time for a signal with several peaks, which controls the peaks that are utilized for rising time and amplitude calculation. In this study, PDT was set to 200 micro-second.

From AE signals, different features are calculated (**Figure 19 b**). For instance, duration is the time between the first threshold crossing and the last threshold crossing. Signal amplitude is the peak of a signal. Signal strength is the integral of the rectified voltage signal over signal time. Rise time is the time between the first threshold crossing and the peak time.



(a) Acoustic emission phenomenon



(b) Acoustic emission signal

Figure 19: AE acoustic emission

5.5 NDE Method – Digital Image Correlation (DIC)

5.5.1 DIC Overview

A research team from Vanderbilt University (VU) was invited to study the concrete test specimens using DIC. DIC is a stereo optical strain measurement system that uses two digital video cameras to capture the motion of a set of reference points, and resolve three-dimensional displacement and strains over the deforming surface. For this test, the reference points are represented by a random speckle pattern that was applied to the surface of the test specimen. The DIC system is comprised of two digital cameras, lighting, and a data acquisition system connected to a computer. The speckle pattern was created by applying paint in a random pattern on the specimen being tested. The pattern is composed of black speckles applied on a white background. See **Figure 20** for images of both the system hardware and a sample speckle pattern.



Figure 20: Digital Image Correlation (DIC) system and speckle pattern

5.5.2 Pattern Application and Imaging

A correctly sized speckle pattern is critical to collecting strain data from the images. The pattern was applied to the UASR specimen using a white acrylic enamel paint for the background and black paint for the speckles. The pattern was 900 mm by 900 mm. See **Figure 21** for an image of the speckle pattern being applied.

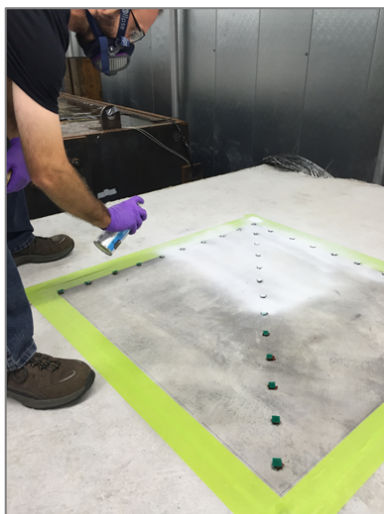


Figure 21: White background paint being applied to UASR specimen

The tripod with the digital cameras was setup on top of the UASR specimen (see **Figure 22**) and was calibrated using a standard 1-meter calibration object. After calibration, the system is ready for taking images of the specimen.



Figure 22: DIC cameras located above the pattern on the UASR specimen

5.5.3 Image Analysis

Once the images are collected, the GOM ARAMIS software allows the user to:

- apply a mask to the image to eliminate areas where there was no pattern applied,
- perform a movement correction which aligns all the images to each other since the data has been collected at different instances of equipment setup,
- insert a 'start point', which is a point of reference for the software to compute the deformation of the specimen.

After completing these steps, the ARAMIS software can then perform the calculations to determine the strain in the UASR specimen. The epsilon X, Y, and XY components of the strain equation can all be shown individually.

5.5.4 Pattern Degradation

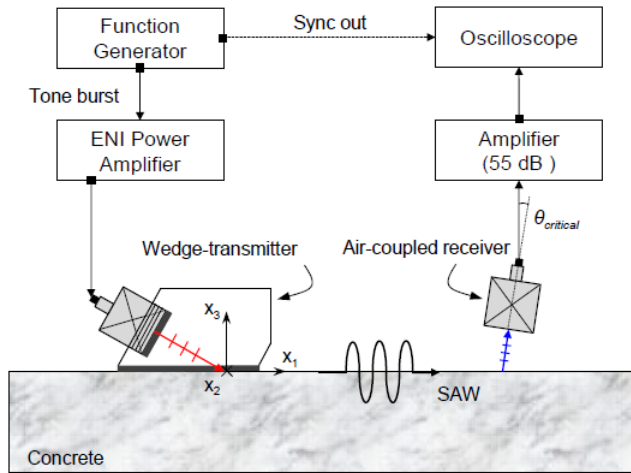
During both the second (Oct. 17th) and third (Dec. 20th) times that data was collected on the UASR specimen, the painted speckle pattern was inspected for damage and degradation. Anytime there is a change in the speckle pattern it results in the DIC system being unable to correlate that part of the pattern with the last image set collected. This loss of data shows up as missing facets on the strain images. Sometime between the pattern application and the second data collection date the pattern was damaged by human interaction, which caused a loss of data mainly in the lower right hand corner of the image. By the third data collection date the pattern was showing some degradation of the black speckles which also resulted in a loss of data. After which, small pattern degradation was present for each visit but only resulted in a small loss of facets.

5.6 NDE Method – Nonlinear Ultrasonic (NLU) Rayleigh Surface Waves

5.6.1 Overview of NLU Method

A research team from the Georgia Institute of Technology (GT) was invited to study the concrete test specimens using a nonlinear Rayleigh surface wave technique. Nonlinear ultrasonic (NLU) techniques measure absolute, baseline reference-free material parameters that can enable accurate and quantitative prediction. In cement-based materials, these NLU techniques are a direct measure of the material's inherent nonlinearity, which is dominated by the nonlinear dynamic behavior of micro-cracks and other damage. These NLU techniques are acoustic wave based, so component interrogation can be performed with bulk, surface and guided waves using the same underlying material physics. The second harmonic generation (SHG) in Rayleigh waves using noncontact air-coupled detection has great potential for in-service monitoring because they only require access to one side of a component. In addition, NLU measurements can be performed relatively quickly allowing relatively large areas to be interrogated, with the long-term possibility of automated or remotely controlled measurements.

The measurement setup used in this research utilized a narrow band contact piezoelectric transducer (with a center frequency of 50 kHz) to excite a longitudinal wave into a Teflon wedge with an angle matched for Rayleigh wave generation in concrete, plus a broadband non-contact, air-coupled receiver centered at 100 kHz (Kim et al., 2018). The signal input is fourteen cycles of a 47 kHz pulse, amplified by an ENI power amplifier by 50 dB to enable the SHG of Rayleigh waves. The measurement setup to generate and detect nonlinear Rayleigh surface waves for the concrete specimens is shown in **Figure 23**.



(a) Schematic of the NLU setup (b) Photo of the NLU measurement system

Figure 23: The NLU measurement setup for nonlinear Rayleigh surface waves

5.6.2 NLU Testing on Concrete Specimens

GT performed testing and analyzed data obtained from the large-scale concrete specimens. A fast Fourier transform (FFT) of a windowed portion of the measured time-domain signal yields the fundamental amplitude labeled A_1 (at 47 kHz) and second harmonic amplitude labelled A_2 (at 94 kHz) (Kim et al., 2018). A connection between the concrete and transducer/wedge source is ensured by use of vacuum grease at a fixed location for the duration of the tests. The air coupled receiver is then moved along the acoustic propagation axis to determine the ratio of $A_2 / (A_1^2 x)$ as a function of the propagation distance, x . The result of this relation is referred to as the relative acoustic nonlinearity parameter, b (Kim et al., 2018). The measured relative acoustic nonlinearity parameter tracks only the nonlinear behavior of the concrete material.

The team from GT performed testing on the concrete specimens at three separate dates: April 21, May 25, and June 17, 2017. For each testing date, the setup was placed on the top of each specimen and three directional measurements were taken: X-direction, Y-direction, and diagonal. The measured relative acoustic nonlinearity parameter was used to compare the different specimens.

5.7 NDE Method – Diffuse Ultrasonic Waves (DUW)

5.7.1 Overview of Diffuse Ultrasonic Waves (DUW) Method

A research team from the University of Nebraska, Lincoln (UNL) was invited to study the concrete specimen using a diffuse ultrasonic wave method. Conventional ultrasonic wave methods measure signal travel times and amplitudes (coherent part only) in the material, and then use ultrasonic velocity and attenuation to estimate quality of concrete. To avoid strong scattering in a highly inhomogeneous and scattering medium like concrete, the ultrasonic wavelength (λ) should be larger than the aggregate (~25mm). Therefore, most conventional ultrasonic methods for concrete NDE use low frequency ultrasounds (<100 kHz). However, low frequency ultrasound cannot accurately characterize concrete degradation at early stages since the wavelengths are much larger than microcracking damage in concrete.

When the wavelengths of ultrasonic waves are smaller than or comparable to the size of scatters (aggregates, cracks), the waves will be scattered multiple times and take a long path before received by

sensors, while the amplitude of coherent part of signal is attenuated. Because the scattering paths are random, the received signal has elongated duration and a noisy tail (coda wave). The diffuse ultrasonic signal contains rich information about the medium because of multiple interactions between scattered waves and scatters (e.g. cracks). Recent studies have shown the potential of diffuse ultrasonic wave methods to evaluate ASR induced microcracking damage in concrete. Another recent study has also shown the high sensitivity of coda wave analysis for monitoring self-healing process of cracking mortar samples. The diffuse signal data can be interpreted through scattered field analysis (diffusivity) or coda wave interferometry (CWI). The CWI method compares late parts of two signals measured at different damage levels and calculates the relative wave velocity change (time delay) between them using correlation method. This analysis method is much more sensitive than the conventional test that measures the time change of first arrivals. It can capture very small changes in specimens caused by microcrack initiation or development, which alters the travel path of coda waves in material. Therefore, the CWI method is especially suitable for continuous monitoring of microcrack development induced by ASR damage in concrete.

5.7.2 Diffuse Ultrasonic Waves Method Testing on Concrete Specimens

The research team from the University of Nebraska, Lincoln first came and installed sensors on the concrete specimens on April 21, 2017. Two transmitters were placed on the top surface of each specimen. Additionally, four receivers were attached to the bottom surface of each specimen. The entire system setup for the concrete specimens is shown in **Figure 24**. In total, these combinations of transmitters and receivers provide eight measurements for each specimen for each measurement time. The measurement system is timed to collect data once per day from 2:10 AM to 2:20 AM. Because these sensors were installed relatively late in the accelerated testing timeline, a significant amount of expansion had already occurred, and very little expansion occurred after installation.

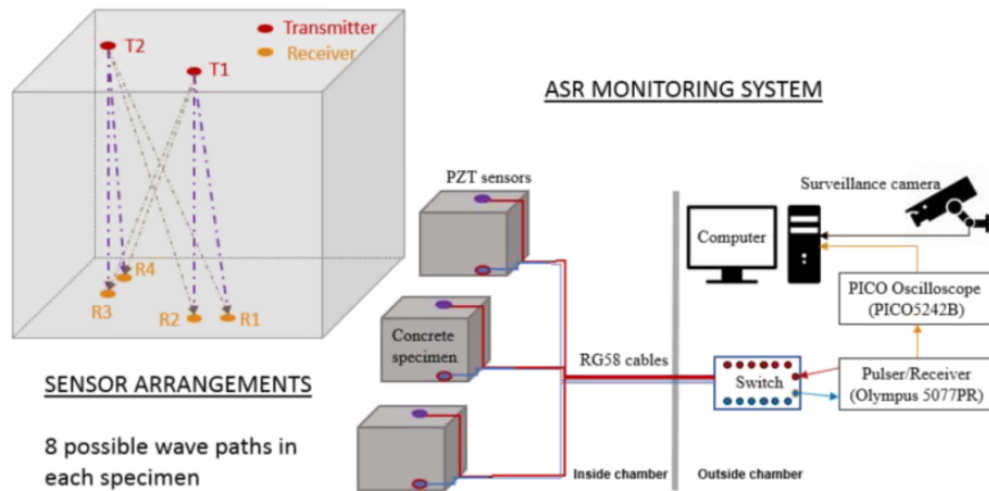


Figure 24: Test setup for diffuse ultrasonic wave method on concrete specimens

The data acquisition system was installed outside of the environmental chamber and connected to sensors inside the chamber on the specimens by sensor cables. The monitoring system and attached sensors are shown in **Figure 25**.



Figure 25: Ultrasonic monitoring system and sensors

6. Results

6.1 Material Testing

6.1.1 Compressive Strength

The average compressive strengths and standard deviations of results for each specimen type at each occurred test date are shown in *Table 4*.

Table 4: Mean and standard deviation (SD) compressive strength of concrete cylinders

Age (Years)	Age (Days)	Compressive Strength, f'_c (MPa)					
		CASR		UASR		CTRL	
		Mean	SD	Mean	SD	Mean	SD
0.02	7	20.6	0.36	17.4	0.70	27.4	1.32
0.08	28	22.2	2.07	20.7	1.17	34.3	1.08
0.25	91	27.2	4.11	24.3	0.52	36.7	0.10
0.39	143	31.1	0.98	26.8	1.03	36.4	1.31
0.50	181	30.9	0.31	27.3	1.03	39.7	0.33
0.75	274	25.9	1.85	25.4	1.10	40.3	2.16
1.00	365	27.6	1.33	27.1	0.96	39.9	1.70
1.50	548	27.9	2.46	27.3	1.084	43.2	1.65
2.00	730	28.5	0.95	28.5	1.88	43.3	0.44

The 28-day compressive strength significantly varies between the concrete mix designs including sodium hydroxide, NaOH (CASR and UASR) and the mix design with lithium nitrate, LiNO_3 (CTRL). Literature supports the conclusion that the addition of NaOH significantly reduces ultimate compressive strength of concrete (Smaoui, Bérubé, Fournier, Bissonnette, & Durand, 2005). Literature also supports the conclusion that the addition of lithium nitrate to the concrete mix can increase ultimate strengths while also increasing rate of strength development (Millard, 2006).

Figure 26 illustrates the average compressive strength from each testing age that has occurred to this date. The error bars indicate one standard deviation above and below the mean. The y-axis of the figure displays compressive strength in mega-Pascal's while the x-axis displays age of concrete in days. Deterioration of compressive strength due to ASR is not noticed until a concrete age of 181 days. However, at 365-day testing age, the compressive strength of both the CASR and UASR specimens increased from the previous value. After approximately one year of accelerated testing, the expansion had plateaued and only small increases in expansion values occurred after that point. As a result, the compressive strength after 365 days does not decrease further. Instead, a small recovery of compressive strength is observed which is consistent with existing literature data (Ahmed, Burley, Rigden, & Abu-Tair, 2003; Gautam, 2016; R. N. Swamy & Al-Asali, 1988).

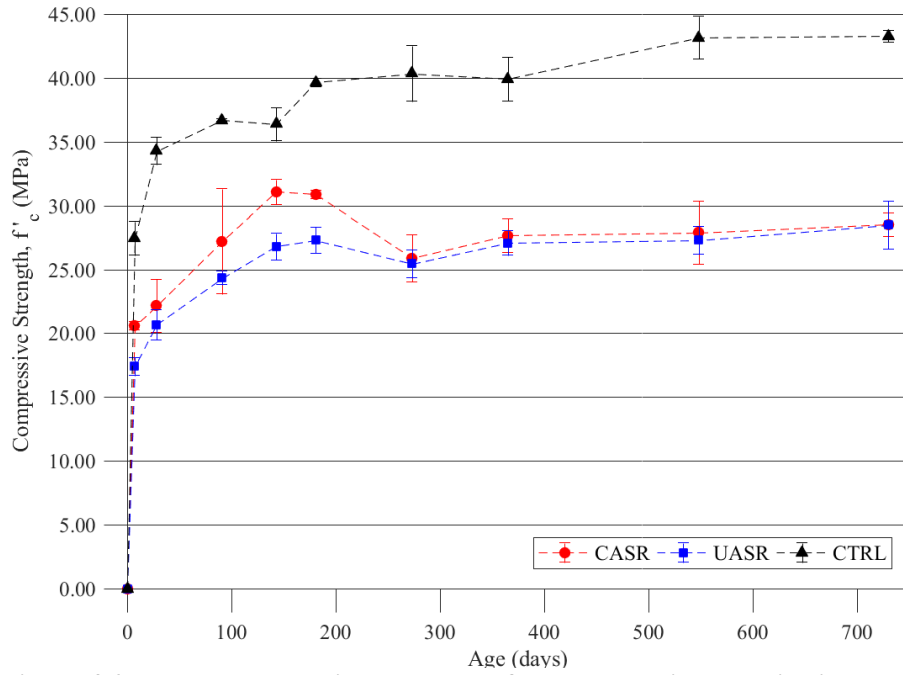


Figure 26: Mean compressive strength of concrete cylinders with increasing age

6.1.2 Elastic Modulus

The mean values for elastic modulus and standard deviation are reported in **Table 5** and illustrated in **Figure 27**.

Table 5: Average and standard deviation of modulus of elasticity of concrete cylinders

Age (Years)	Age (Days)	Elastic Modulus , Ec (GPa)					
		CASR		UASR		CTRL	
		Mean	SD	Mean	SD	Mean	SD
0.02	7	34.0	3.94	34.0	0.00	34.4	1.58
0.08	28	33.7	3.03	33.2	2.22	34.4	0.05
0.25	91	30.8	1.02	30.0	0.54	37.2	0.34
0.39	143	26.6	1.45	21.9	0.21	36.2	0.27
0.50	181	24.5	2.79	18.0	0.90	39.8	1.47
0.75	274	22.3	2.96	17.1	2.43	41.3	1.10
1.00	365	25.3	0.72	15.0	1.77	41.7	2.50
1.50	548	25.4	0.65	16.7	1.50	41.7	0.69
2.00	730	25.6	0.06	15.0	0.78	40.5	0.35

Figure 27 illustrates the average elastic modulus from tests that have occurred to this date. The y-axis of the figure displays elastic modulus in giga-pascals while the x-axis displays age of concrete in days.

CASR and UASR material testing specimens have tested at lower values of elastic modulus when compared to CTRL specimens as time has progressed. Also, UASR specimens have tested at lower values of elastic modulus when compared to CASR specimens as time has progressed. These two observations can lead to two preliminary conclusions. First, ASR reduces the elastic modulus of cylindrical concrete specimens which is also supported in the literature (Larive, Laplaud, & Joly, 1996) (Giaccio, Zerbino, Ponce, & Batic, 2008). Second, concrete specimens in the unconfined boundary condition are subject to more deterioration of elastic modulus when compared to the same concrete in the confined condition; however, no literature reporting elastic modulus of confined concrete specimens subjected to ASR could be found at this time to support this conclusion. As the reaction progresses, it is expected that deterioration will even further decrease the elastic modulus of the CASR and UASR specimens. Again, nearing 365-day when expansion has flattened, the deterioration of elastic modulus has also flattened.

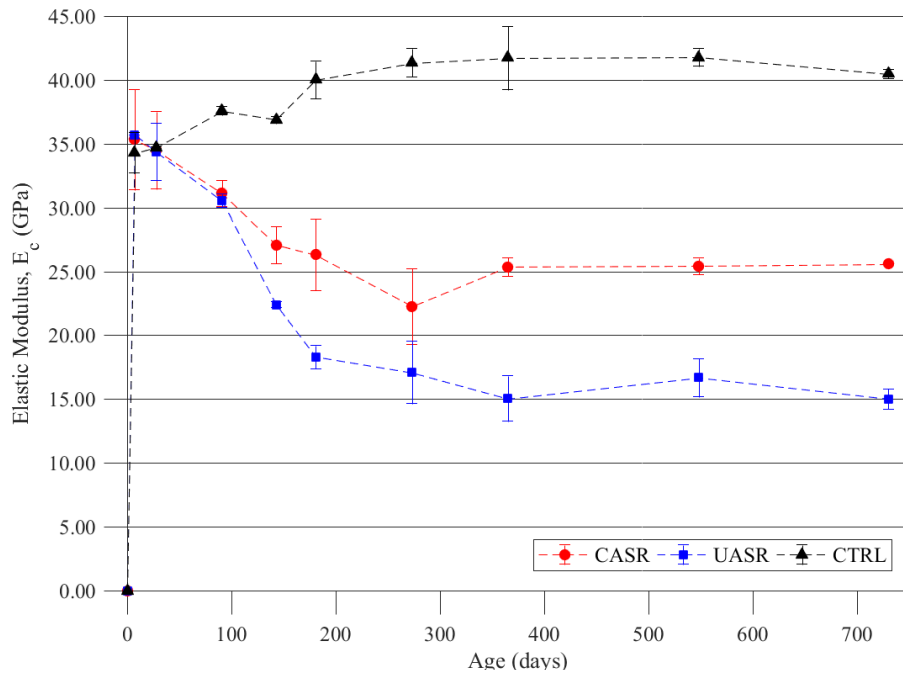


Figure 27: Mean elastic modulus of concrete cylinders with increasing age

6.1.3 Splitting Tensile Strength

The tabulated values for the split tensile strength are shown in **Table 6**. **Figure 28** illustrates the average elastic modulus from tests that have occurred to this date. The y-axis of the figure displays split tensile strength in mega-pascals while the x-axis displays age of concrete in days. After expansion has plateaued, a slight recovery of split tensile strength back to original strength is observed.

Table 6: Average split tensile strength of concrete cylinders

Age (Years)	Age (Days)	Tensile Strength, f'_t (MPa)					
		CASR		UASR		CTRL	
		Mean	SD	Mean	SD	Mean	SD
0.08	28	2.7	0.21	2.13	0.04	3.18	0.13
0.25	91	2.65	0.09	2.48	0.13	3.26	0.32

0.50	181	2.43	0.17	2.38	0.19	3.53	0.12
0.75	274	2.22	0.04	2.18	0.27	3.11	0.05
1.00	365	2.37	0.05	2.49	0.36	3.21	0.33
1.50	548	2.30	0.31	2.67	0.21	3.21	0.23
2.00	730	2.23	0.16	2.67	0.17	3.74	0.20

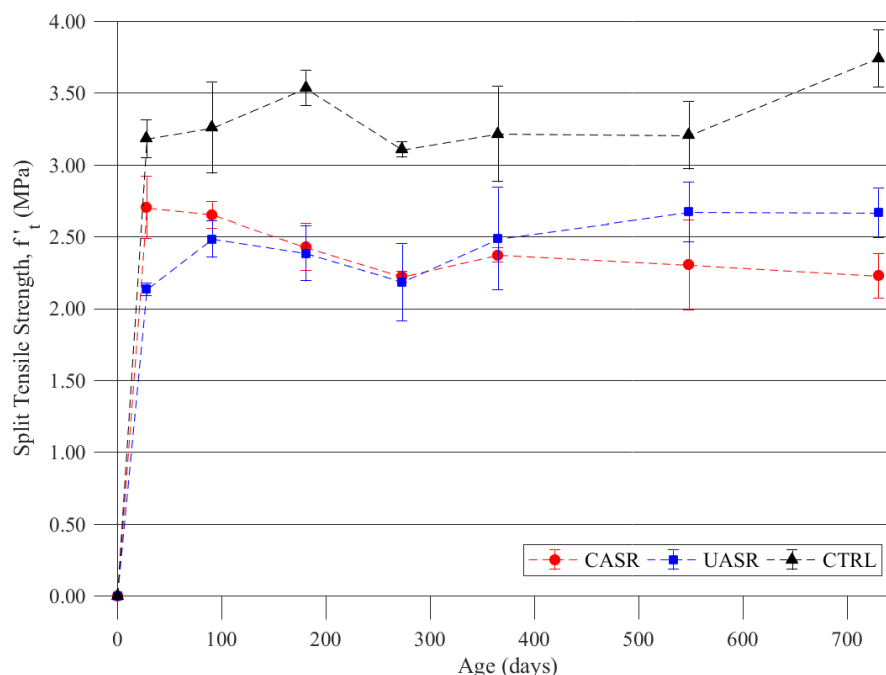


Figure 28: Mean splitting tensile strength of concrete cylinders with increasing age

6.2 Strain and Deformation Monitoring

6.2.1 Early Concrete Age

The internal temperature history of each specimen is shown in *Figure 29*. The reported temperature for each specimen is the recorded maximum of the four thermocouples embedded in that specimen. The CASR and UASR specimens were cast first in the early morning, and the CTRL specimen was cast after midday when the temperature within the lab was higher. For all specimens, the internal temperature remained below 70 °C, which prevents the occurrence of DEF in the specimens. The temperature of each specimen slowly decreased from the peak of hydration heat stabilizing to room temperature of the laboratory over a period of nearly 20 days, thus minimizing the risk of thermal cracking.

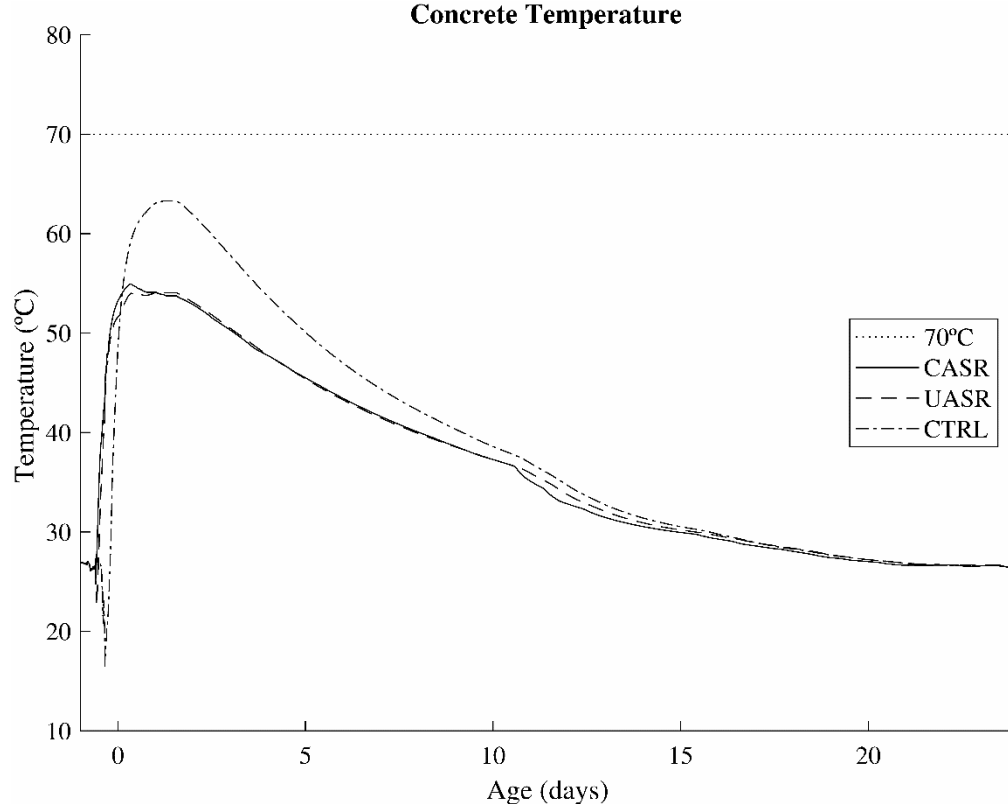


Figure 29: Early age concrete temperature (Hayes et al., 2018)

6.2.2 Sensor Correlation

Despite the differences in the main two sensor systems (gauge-length in particular), the expansion results obtained between the two types of sensors are very agreeable. **Figure 30** and **Figure 31** show the correlation between the local strain transducers and structural deformation sensors oriented to measure strain and deformation in the through-thickness (Z) direction for the CASR and UASR specimens. The mean of the transducer strain is plotted against the structural deformation. The standard deviation (SD) lines indicate one standard deviation above and below the mean strain collected from the local strain sensors. The identity line designates perfect correlation. The linearity of the correlation plots indicates a good correlation between the short and long gauge-length sensors in collecting expansion data. Hence, in the following sections, only the local strains collected by the embedded strain sensors are reported and analyzed.

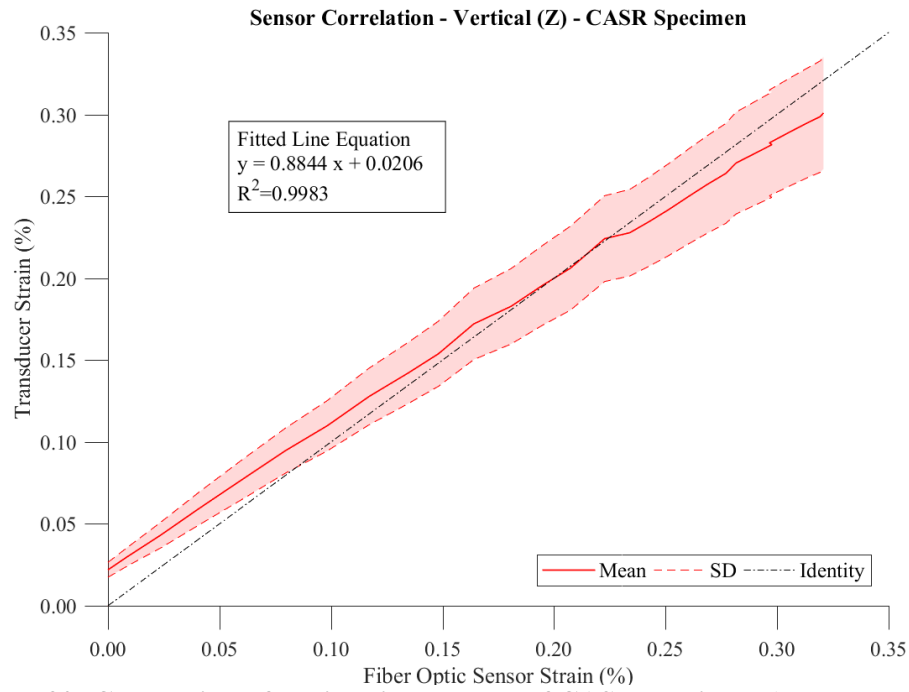


Figure 30: Correlation of Z-direction sensors of CASR specimen (Hayes et al., 2018)

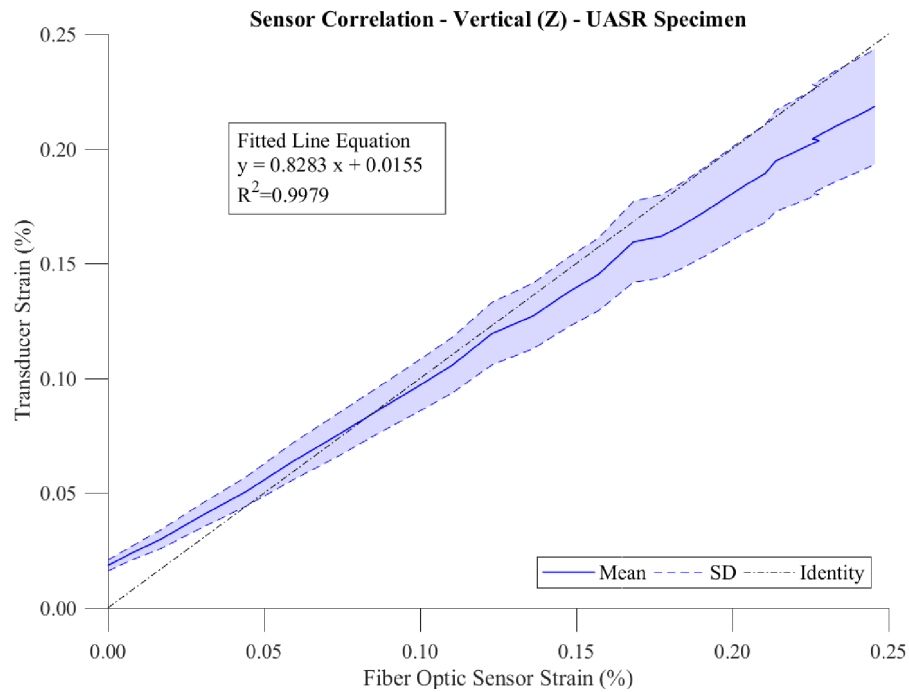


Figure 31: Correlation of Z-direction sensors of UASR specimen (Hayes et al., 2018)

6.2.3 ASR-Induced Expansion

The expansion collected by the embedded strain sensors for each specimen in each direction is shown in **Figure 32**. For the sake of readability, only the average expansions are plotted. The CTRL specimen exhibits relatively low shrinkage and no trend towards expansion. The CASR specimen shows more vertical expansion and less lateral expansion than the UASR specimen. Because of the longer span of the steel confinement frame resisting Y-direction expansion, more deflection would be expected in this direction when compared to the X-direction if the pressure exerted by the ASR-induced expansion is relatively uniform; this reasoning would explain the differences in the Y-direction and X-direction of the CASR specimen.

The volumetric expansion of the two reactive specimens is shown in **Figure 33**. Other studies have concluded that ASR-induced volumetric expansion is independent of stress state or boundary conditions when at least one direction is unloaded or unrestrained (Gautam, Panesar, Sheikh, & Vecchio, 2017; Stéphane Multon & Toutlemonde, 2006). The volumetric expansion of the two reactive specimens is nearly equivalent after one year of accelerated testing confirming these conclusions even for large-scale specimens.

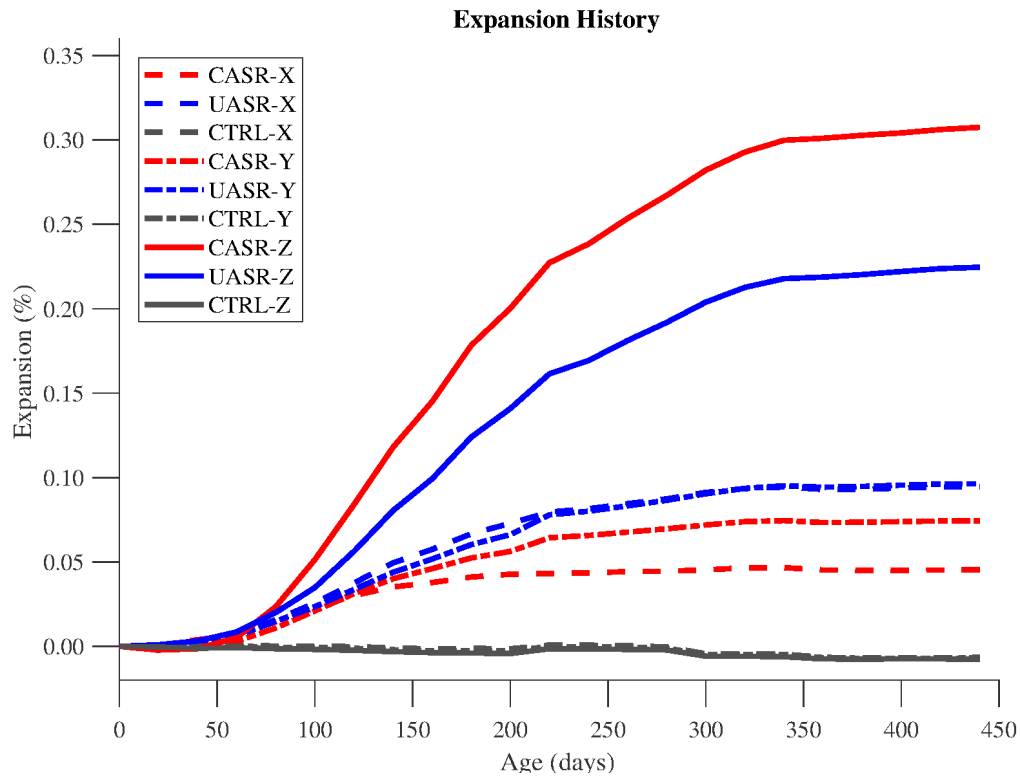


Figure 32: Expansion of each specimen in each direction (Hayes et al., 2018)

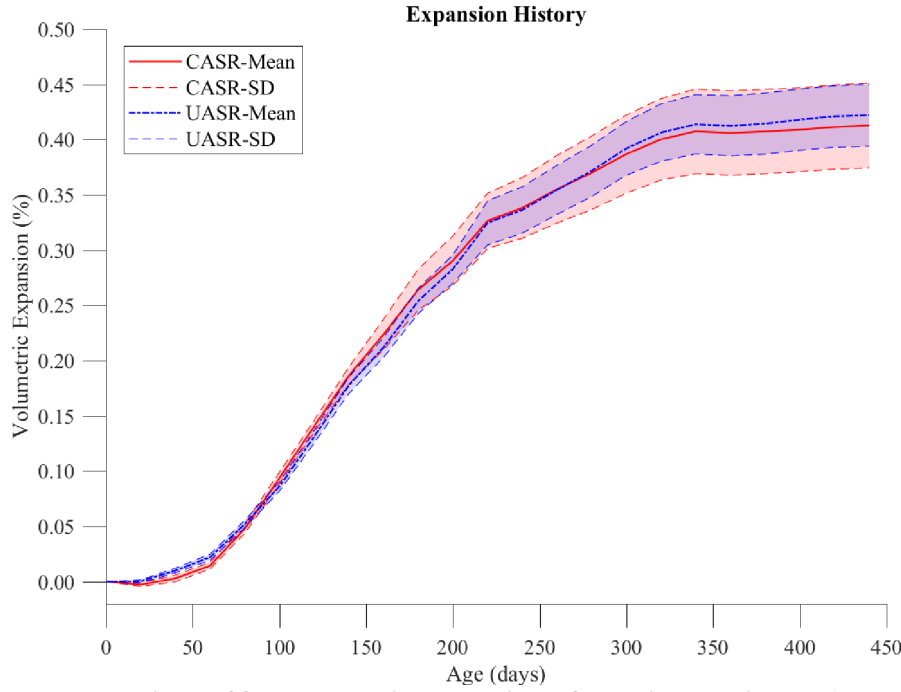


Figure 33: Volumetric expansion of reactive specimens (Hayes et al., 2018)

6.3 NDE Method – Acoustic Emission (AE)

6.3.1 Volumetric Strain Rate

The specific range of volumetric strain data used for comparison and the volumetric strain rate, calculated from the data presented in **Figure 33**, are shown in **Figure 34**. **Figure 34 a** shows the average volumetric strain for the confined, unconfined, and control specimens. It also details the standard deviations of strains for confined and unconfined, which are indicated by Confined \pm SD and Unconfined \pm SD, respectively. The volumetric strain rate in terms of specimen age is presented in **Figure 34 b**. The strain rate was abruptly increased from the casting day up to 120 days and decreased afterwards. The volumetric strains reached plateaus at the end of shown age. The AE data between 50 to 195 days are considered for studying in this report due to the large strain variation. The considered time interval is shown in **Figure 34 a** with two vertical dashed lines.

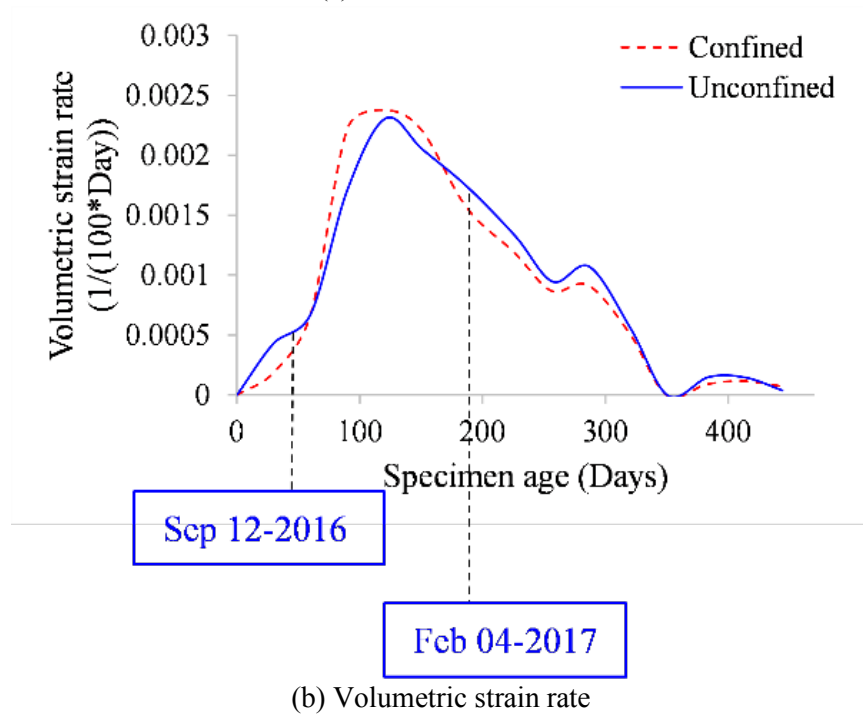
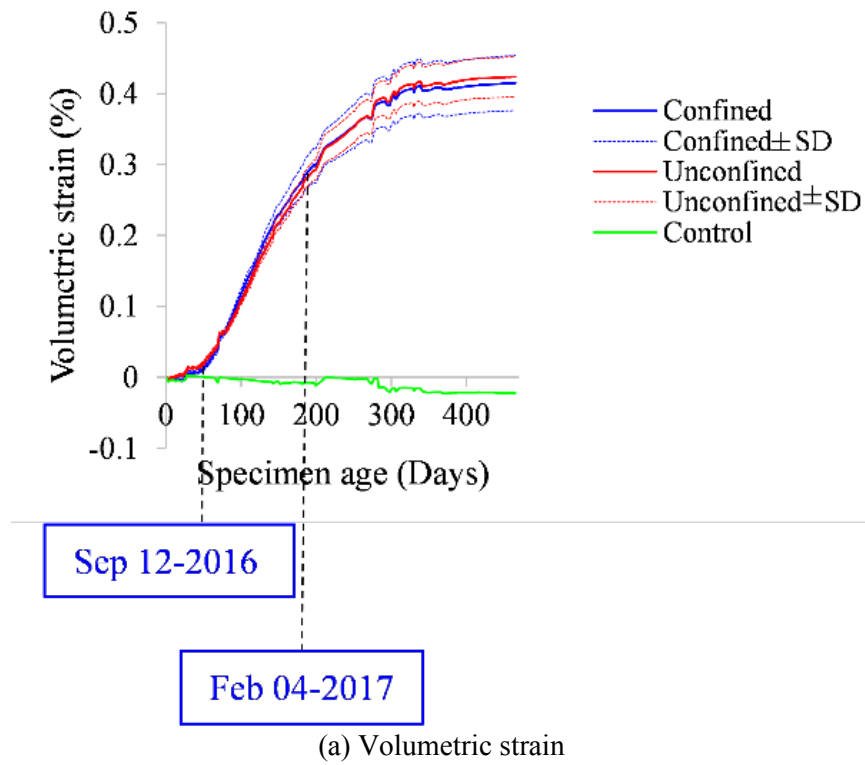


Figure 34: Volumetric strain and rate

6.3.2 Data Filtering

AE data usually contains a large amount of non-relevant signals. To minimize non-genuine data, the data should be passed through several filters. In this study, two different filtering procedures were

developed for data of the broadband and resonant sensors, due to different properties and locations of the sensors. Resonant sensors are highly sensitive and were attached to the bottom surface of the specimens. On the other hand, broadband sensors were embedded in the concrete blocks and much less sensitive than the resonant sensors. Therefore, resonant sensors were highly exposed to the environmental noises than broadband. Suspicious data were removed according to the chamber timetable, control specimen, and waveform inspection. The AE data below 41dB and 32 dB from the resonant and broadband sensors were removed, respectively. Then, the duration versus amplitude distributions were evaluated in order to eliminate the outliers based on a Swansong II filter (ElBatanouny et al., 2014).

This filter is based on the fact that genuine signals with long duration should have the larger amplitude. Therefore, signals with long duration and low amplitude were deleted by visual inspection of the waveforms. This filter was conducted separately on the data recorded by the resonant and broadband sensors and conservative limit ranges were selected based on the limits of reactive specimens. The duration-amplitude filter limits for the resonant and broadband sensors are presented in **Table 7**. A similar concept is applicable for rise time versus amplitude, where signals with low amplitude should have low rise time. The outliers in rise time-amplitude distribution were also eliminated for both resonant and broadband sensors. Rejection limits of rise time-duration distributions were not determined, since the deleted data was small. The filters were applied to the data of three specimens.

Table 7: Duration amplitude rejection limits

External Sensor		Internal Sensor	
Amplitude (dB)	Duration (ms)	Amplitude (dB)	Duration (ms)
41-43	400<	32-35	155<
44-45	500<	36-42	260<
46-47	600<	43-100	330<
48-49	650<	-	-
50-53	820<	-	-
54-56	940<	-	-
57-65	1080<	-	-
66-100	1400<	-	-

6.3.3 Results

Figure 35 presents the cumulative signal strength (CSS) and amplitude of AE data in terms of time after filtering for both the external and internal sensors. The gap in the AE data shows missing data for 38 days. Although CSS distribution for the confined specimen is more gradual than the unconfined specimen, the final CSS values for both reactive specimens are very close. The control specimen was illustrated in **Figure 35 c**. The amount of data is much less than the reactive specimens. Moreover, final CSS is less than 500,000 pVs (picovolt second), which is much less than the values for the reactive specimens, illustrating different potential damage trends between the reactive specimens and control specimen. The reactive specimens had a reactive aggregate with NaOH solution, which made it different from the control specimen.

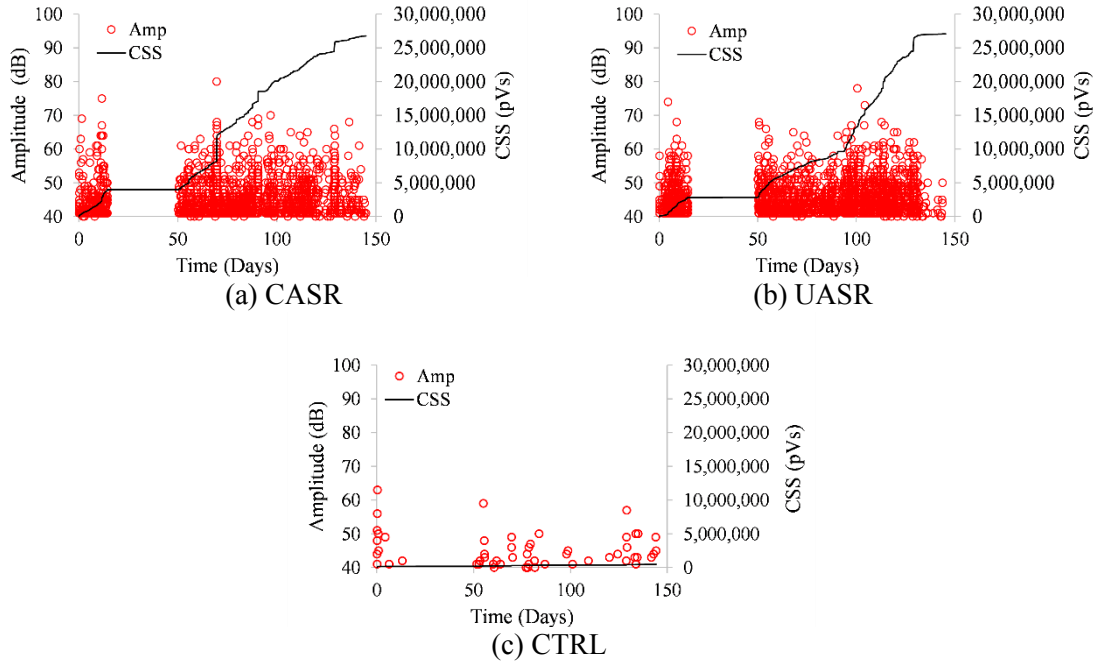
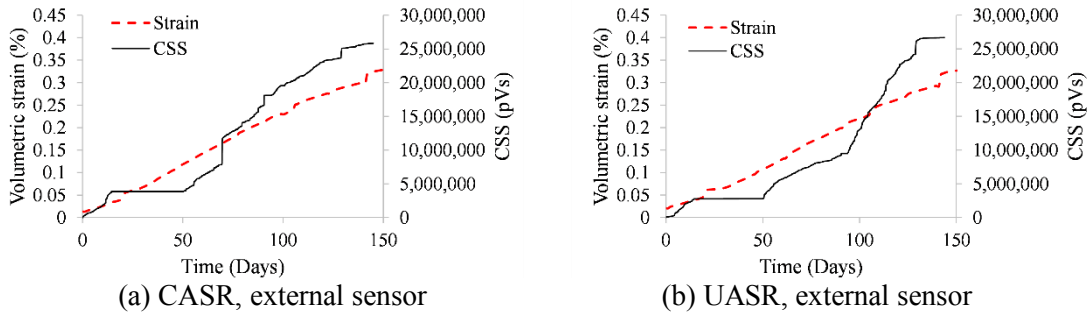


Figure 35: Amplitude and CSS versus time

The volumetric strain versus CSS in terms of time is presented in **Figure 36**. There is an almost linear correlation between CSS and volumetric strain. The correlation coefficients for the confined specimen between strain and CSS are 0.96 and 0.94 for the external and internal sensors respectively; CSS increases as the reactive specimens expand. The expansion inside the specimens exceeded the tensile strength of concrete and this led to crack and damage progression in the specimens, which were recorded by AE sensors. The difference between the CSS curves of the reactive specimens for the internal sensors may be due to different damage mechanisms inside the specimens. The crack openings are expected, and supported by expansion data, to be primarily limited to through-thickness for the confined specimen due to the imposed confinement. According to **Figure 35** and **Figure 36**, AE has a reasonable capability to monitor the damage progression caused by ASR in terms of time by use of the CSS.



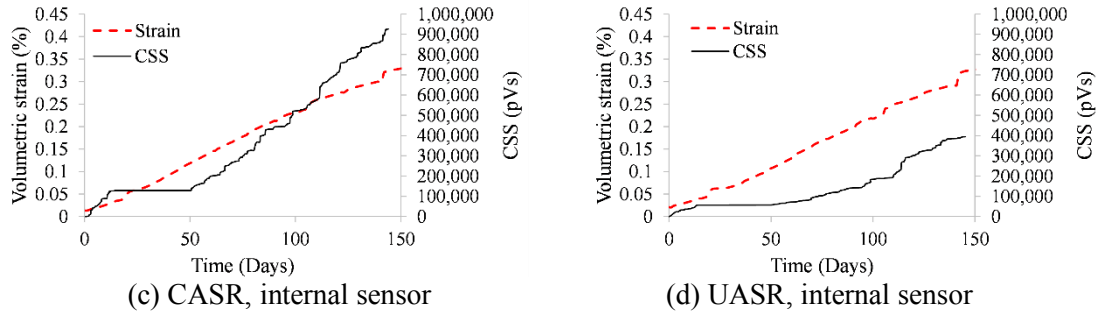


Figure 36: Comparison of CSS and expansion

6.3.4 Damage Index

Improved b-value (Rao & Lakshmi, 2005), historic index, and severity are utilized for damage identification using AE data. The improved b-value for each specimen is shown in **Figure 37**. b-value indicates the times associated with damage in the specimens (shown by the circles in the figure). The CSS rate in these times increases abruptly. However, b-value cannot be a good damage index for comparing between the specimens due to neglecting the cumulative nature of the damage.

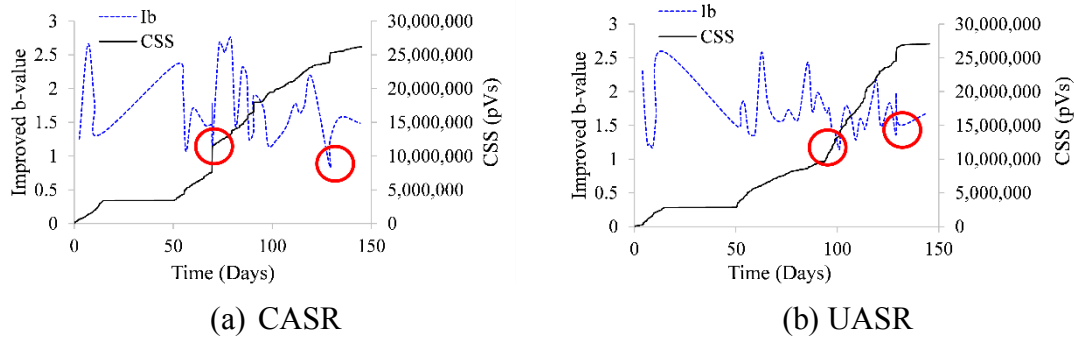


Figure 37: b-value

Intensity analysis was conducted on the data using two parameters of historic index and severity. The historic index is a cumulative signal strength rate and severity is the average signal strength of the fifty larger hits in the specific time window (Abdelrahman et al., 2015). These two parameters are presented in logarithmic scale. The result of intensity analysis is presented in **Figure 38**. The intensity parameters were calculated for 30, 60, 90, and 145 days for the reactive specimens. For the control specimen, the parameters were calculated for 145 days.

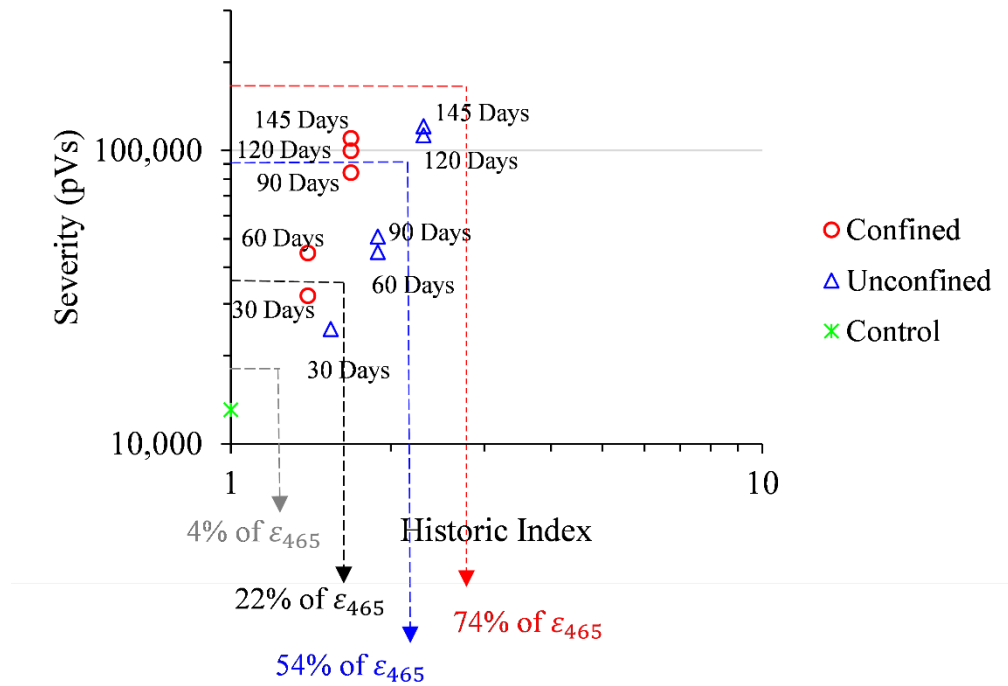


Figure 38: Intensity analysis

Figure 38 is separated to the regions based on associated volumetric strain percentages. These values were calculated in terms of final volumetric strain for 465 days according to **Figure 34**. As seen, the intensity values have a correlation with the volumetric strain percentages. Since a larger volumetric strain reflects a larger damage level, the intensity values can be attributed to the level of damage. The points on the upper right side of the figure illustrate higher damage levels than the points on the lower left side of

the figure. Therefore, a higher potential damage for the reactive specimens is predictable compared to the control specimen.

6.4 NDE Method – Digital Image Correlation (DIC)

6.4.1 Measured Strains

Table 8 shows DIC calculated strains for several of the investigation times as reported by the team at Vanderbilt University. It is worth noting that since April 2018 (concrete age of 272 days), DIC calculated strain values have changed very little which is consistent with permanent strain monitoring data of the X-direction and Y-direction sensors. The table also shows the number of facets and facet percent loss between measurements which indicate a loss of data likely due to degradation of the pattern on the concrete. In two instances, facets were gained between two consecutive measurements which was likely due to increased lighting while the image was taken.

Table 8: DIC measured surface strains and facets

Date	Concrete Age	ϵ_x (%)	ϵ_y (%)	Facets	% Facet Loss
08/08/2016	15	-	-	15021	0
10/17/2016	85	0.109	0.132	14699	2.14
12/12/2016	141	Bad data	-	-	-
02/17/2017	208	0.193	0.224	14644	2.51
04/22/2017	272	0.161	0.178	14545	3.17
06/28/2017	339	0.158	0.175	14683	2.25
08/24/2017	396	0.151	0.170	14806	2.10
10/19/2017	452	0.143	0.162	14532	3.26

Figure 39 and **Figure 40** show the progression of the strain field for the X-direction and Y-direction respectively. As shown, the strain increased significantly between October 2016 and February 2017 as supported by the measured strains. The remaining progression after this point is much slower. Additional measurements were taken every two months after October 2017, however; there was very little change in the measured strains.

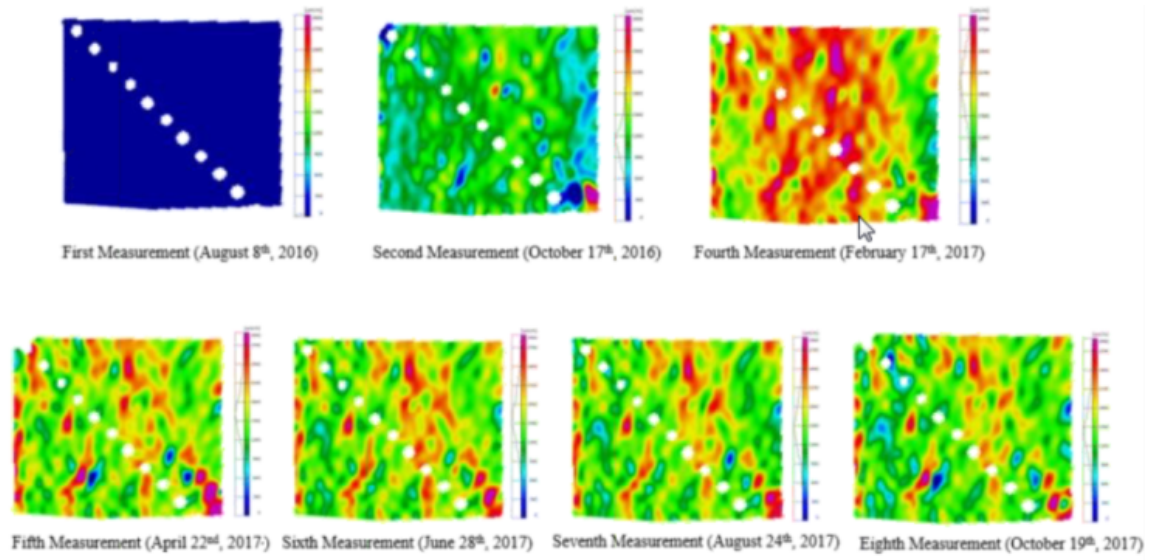


Figure 39: Progression of DIC strain images for strain in X-direction

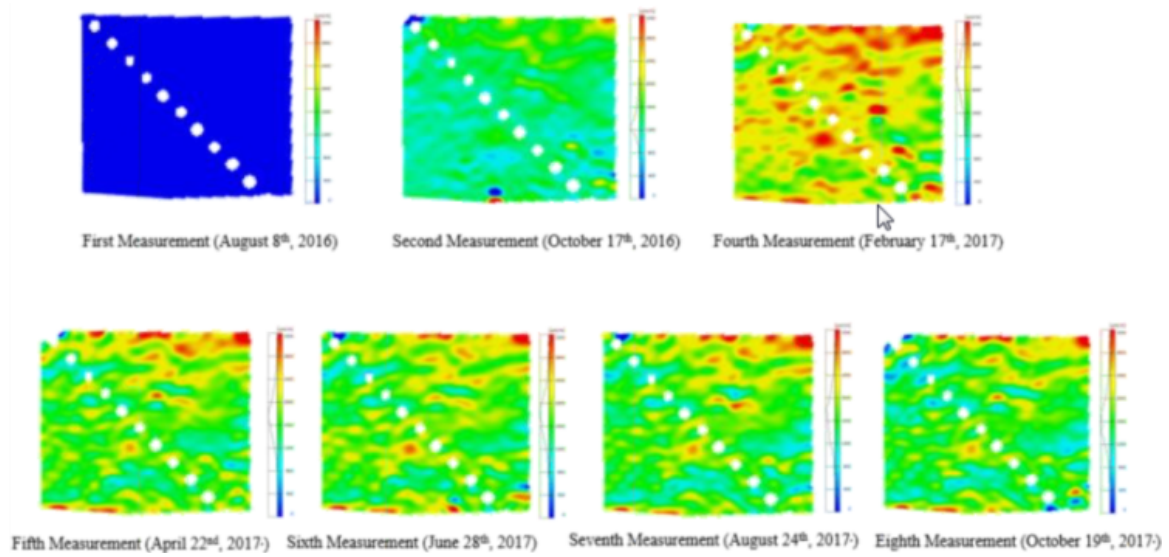


Figure 40: Progression of DIC strain images for strain in Y-direction

6.5 NDE Method – Nonlinear Ultrasonic (NLU) Rayleigh Surface Waves

6.5.1 Relative Acoustic Nonlinearity Parameter

Figure 41 illustrates the measured relative acoustic nonlinearity parameter, b , obtained for each specimen by the NLU Rayleigh surface wave technique as reported by the team at Georgia Institute of Technology. The b value is an indicator of the ASR-induced microscale damage. Values in the figure are relative to the measurement of the CTRL specimen at first measurement. No visible surface cracking was observed at any measurement time within the monitoring region. Therefore, the increase in b values could indicate an increase in the internal microcracking near the surface. The b values for the two reactive specimens are notably higher than the CTRL specimen values with UASR values being higher than CASR specimen values. **Table 9** through **Table 11** show the measured directional b values with corresponding levels of directional expansion of the large-scale concrete specimens. A measurement of “N/A” indicates that there was significant scattering of fundamental and second harmonic Rayleigh wave contributions likely due to excessive micro-cracking within the evaluation area.

As shown the nonlinearity parameter, increases with increasing expansion, but also slightly increases as the CTRL specimen experiences slightly more shrinkage which may be due to the formation of shrinkage cracks.

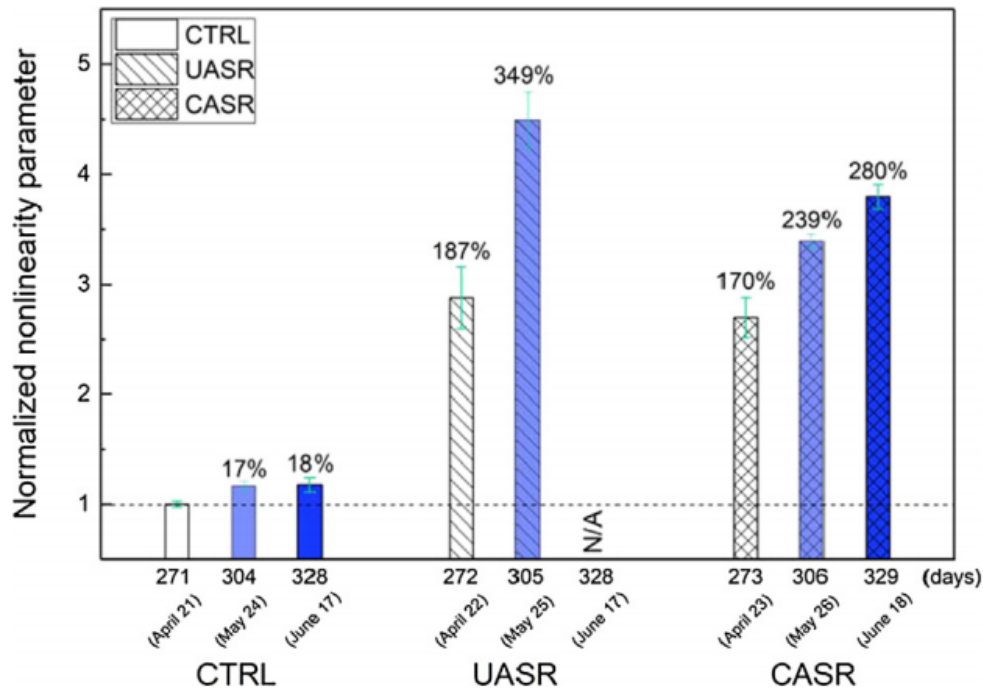


Figure 41: Summary of measured b values for the CTRL, UASR, and CASR specimens normalized to day 271 CTRL value (Kim et al., 2018)

Table 9: Summary of measured expansion and b: CTRL specimen (Kim et al., 2018)

Day	Expansion (%)			b (x10 ⁻⁶)
	X-dir.	Y-dir.	Avg.	Avg.
271	-0.0016	-0.0023	-0.0020	0.445
304	-0.0045	-0.0048	-0.0047	0.519
328	-0.0043	-0.0046	-0.0045	0.524

Table 10: Summary of measured expansion and b: CASR specimen (Kim et al., 2018)

Expansion (%)				b (x10 ⁻⁶)				
Day	X-dir.	Y-dir.	Avg.	Day	X-dir.	Y-dir.	Diag.	Avg.
271	0.0429	0.0682	0.0556	273	1.14	1.10	1.36	1.20
304	0.0467	0.0737	0.0602	306	1.51	1.46	1.55	1.51
325	0.0470	0.0747	0.0609	329	1.62	1.57	1.88	1.69

Table 11: Summary of measured expansion and b: UASR specimen (Kim et al., 2018)

Expansion (%)				b (x10 ⁻⁶)				
Day	X-dir.	Y-dir.	Avg.	Day	X-dir.	Y-dir.	Diag.	Avg.
271	0.0857	0.0850	0.0854	272	1.07	1.86	0.91	1.28
304	0.0928	0.0929	0.0929	305	2.24	N/A	1.73	1.99
325	0.0945	0.0953	0.0949	328	N/A	N/A	N/A	N/A

6.6 NDE Method – Diffuse Ultrasonic Waves (DUW)

6.6.1 Effect of ASR on Relative Wave Velocity and Temperature Relationship

Because the DUW setup was installed in April 2017 (concrete age of roughly 270 days), the DUW method monitoring began after the primary period of expansion due to ASR. The timing of this installation presented a unique opportunity in which the DUW method was used to try to assess the presence of ASR damage after expansion had already occurred. The team at the University of Nebraska, Lincoln first noticed the difference in time domain signals for the three specimens shown in **Figure 42**. The time domain signals differ for each specimen. The CTRL exhibits a high amplitude wave with slow decay. The UASR specimen exhibits a low amplitude wave with a slow decay. The CASR specimen exhibits a high amplitude wave with fast decay. The interpretation of these differences in time domain signals will require additional research to form conclusions.

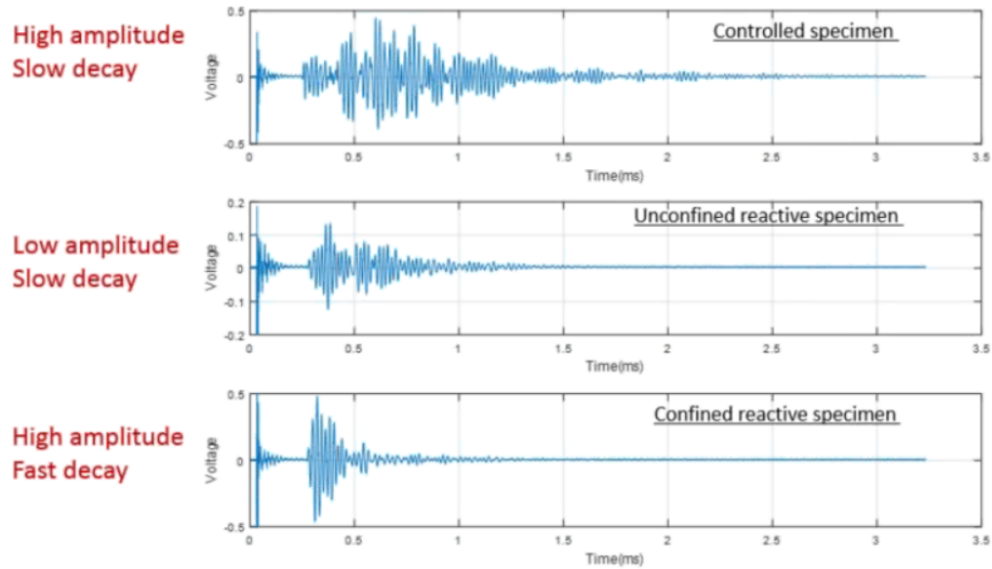


Figure 42: Representative time domain signals for each specimen

Additionally, the presence of ASR damage was found to have an effect on the relative velocity change/temperature relationship. As temperature decreases, the relative wave velocity increases. However, analysis of the relative velocity change as a function of temperature for each specimen yielded different relationships between the two parameters. **Figure 43** shows the relative velocity change plotted against the temperature for each of the three specimens. The significant finding is that the more damaged reactive specimen exhibits a larger change in relative wave velocity with a change in temperature; i.e. the slope of the relative velocity change/temperature relationship increases with pre-existing damage due to ASR. Additional research is required to investigate this effect of the relationship and whether or not it can be used to detect the presence of ASR even after damage has occurred.

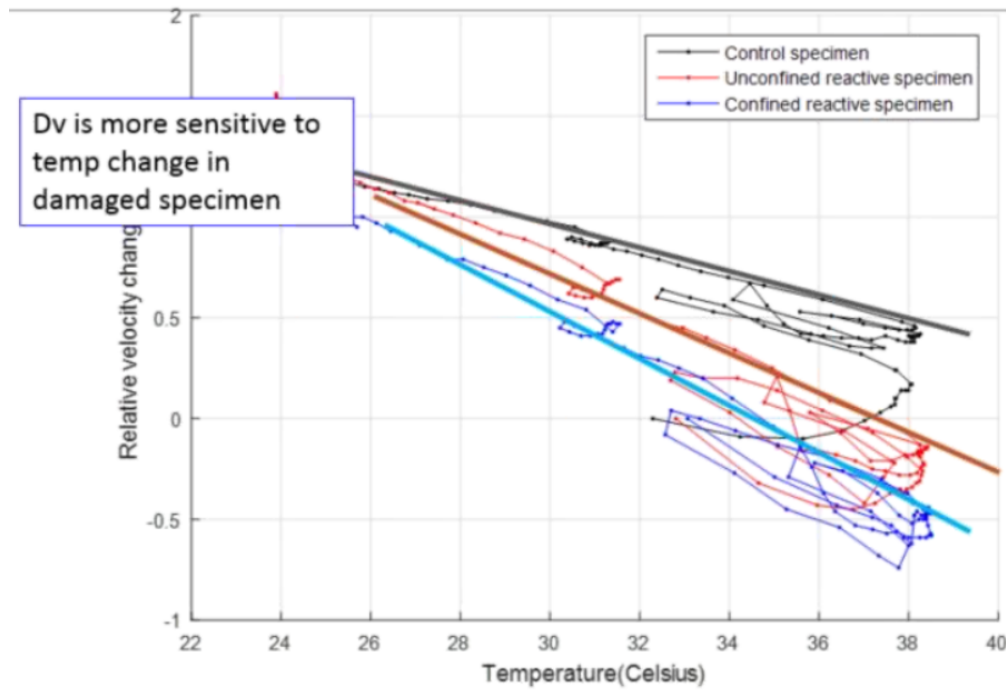


Figure 43: Relative velocity change as a function of temperature

8. Discussion of Results

8.1 Expansion Monitoring – Significance for In-Situ Conditions Assessment

8.1.1 Visual Inspection

Visible cracking first occurred on the lateral sides of the UASR specimen with an early (≈ 150 days) primary crack orientation indicating a preferred direction of expansion through the thickness, in agreement with the measured strains (Hayes et al., 2018). At later stages, branching and pattern-cracks developed on the sides as shown in **Figure 8**. Limited and hardly discernible cracking could be observed on the top surface of the UASR specimen after ≈ 300 days. **Figure 44** shows timings of first observations of visible cracking on the UASR specimen and corresponding levels of expansion. However, no cracking was observed on the top surface of the CASR after 2 years of accelerated testing and significant levels of volumetric expansion.

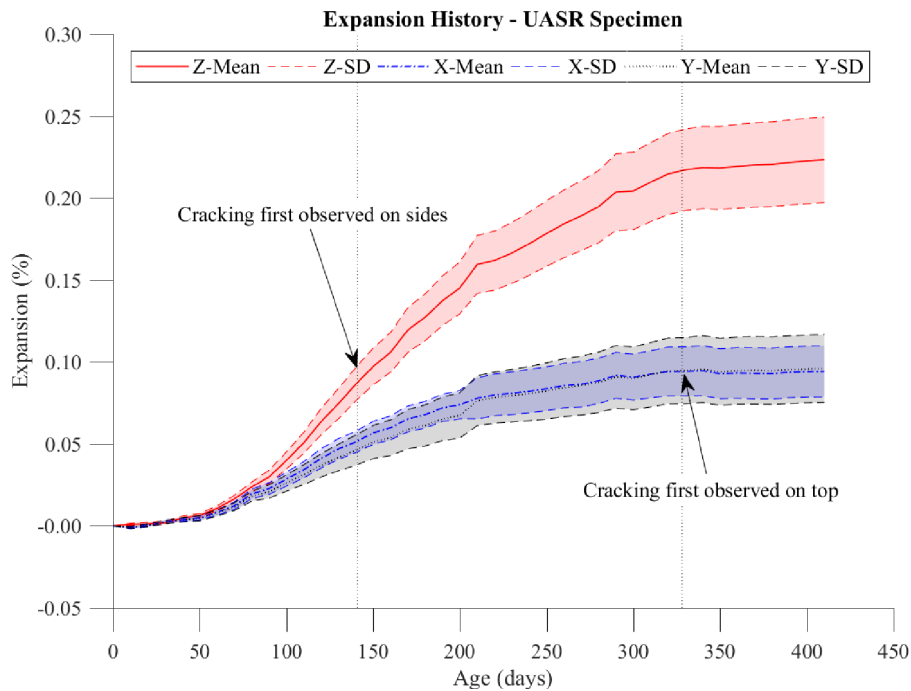


Figure 44: Expansion history of UASR specimen with first cracking observations (Hayes et al., 2018)

In a NPP containment structure, the cracking that would occur generating through-thickness expansion would not be observable as containment structures are typically continuous walls, and hence, the thickness plane is not accessible similar to the CASR specimen in this research.

As a result, assuming that the development of ASR-induced cracking follows a similar chronology in the field, visual inspection may not be a reliable approach to diagnose the presence of ASR in concrete structures without transverse reinforcement until later stages of the reaction after significant levels of expansion have already occurred (Hayes et al., 2018).

8.1.2 Sensors Resilience

The high moisture content, fairly high-temperature, and high-alkalinity of the operating environment poses a significant challenge to the durability of the sensors. Of the 64 strain transducers and 12 long-

gauge FO extensometers embedded in the specimen or attached to the surface of concrete, only one long-gauge FO sensor was lost as a result of unrelated construction works of the environmental chamber.

The long-gauge FO deformation sensors have proven to be a rugged and robust sensor. Three conclusions for these sensors can be made from the monitoring campaign: (1) the sensors are resilient to the harsh environment presented by the environmental chamber; (2) the sensors are easily affixed to concrete surfaces; (3) the sensor measuring device and software are reliable and simple to use (Hayes et al., 2018). For these reasons, the long-gauge FO deformation sensors have strong potential for field implementation as an automated method to track residual expansion of ASR-affected structures.

8.1.3 Expansion Anisotropy

The macroscopic expansion measured on both reactive specimens is strongly anisotropic. While this can be attributed, to some degree, to the casting direction of the concrete specimens (Nizar Smaoui, Bérubé, Fournier, & Bissonnette, 2004), most of the anisotropy of the macroscopic expansion measured in the present research stems from the boundary condition (steel confinement frame) and reinforcement layout. **Figure 45** presents both CASR and UASR vertical (Z) expansions as a function of one-third volumetric expansion. **Figure 46** shows the CASR and UASR expansion in the X direction as a function of one-third volumetric expansion. On both figures, the identity line represents a situation of perfectly isotropic expansion.

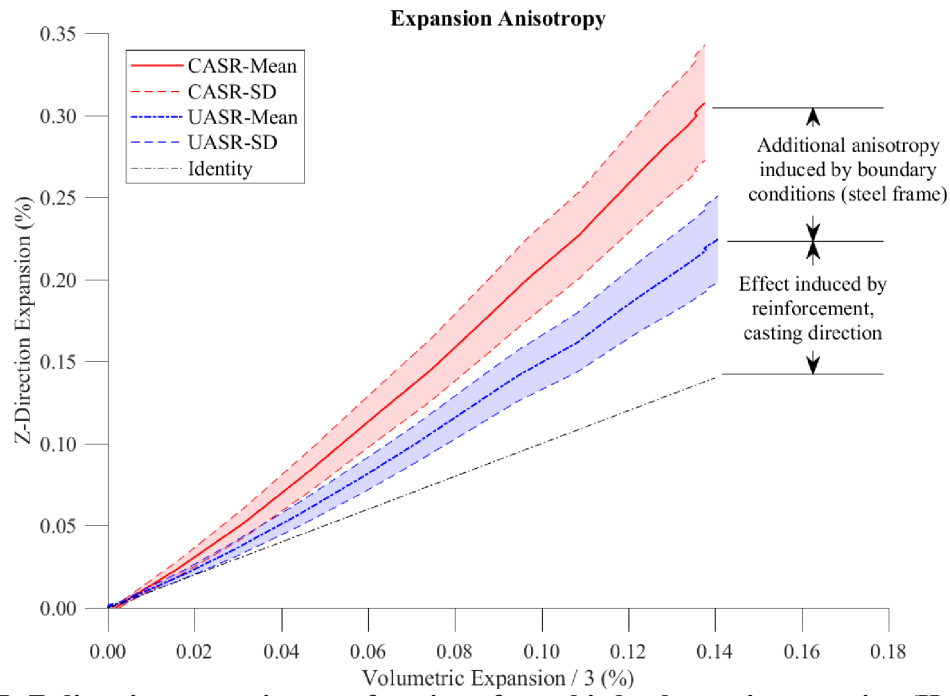


Figure 45: Z-direction expansion as a function of one-third volumetric expansion (Hayes et al., 2018)

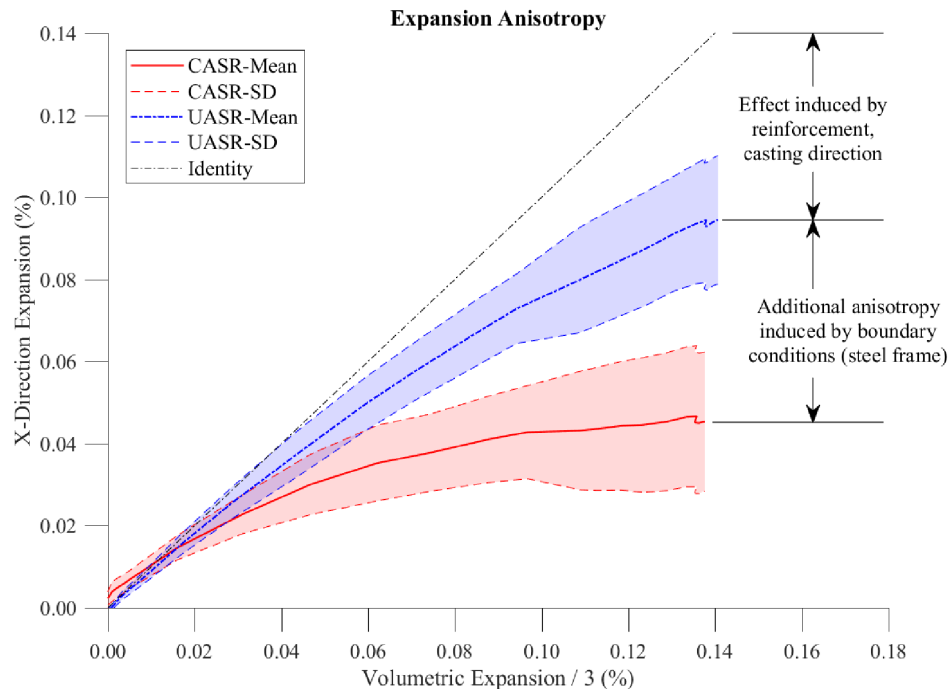


Figure 46: X-direction expansion as a function of one-third volumetric expansion (Hayes et al., 2018)

Both specimens exhibit anisotropic expansion with a preferred direction along the thickness of the specimens (Z). For the UASR specimen, this anisotropic expansion is caused by the difference in reinforcement ratio between the in-plane directions (X,Y) and through-thickness direction (Z) in addition to the preferred expansion attributed to casting direction. For the CASR specimen, the anisotropic expansion is caused by both the reinforcement and the passive restraint from the steel confinement frame, the latter accounting for a 33% increase in vertical (Z) expansion compared to the UASR specimen after one year of accelerated testing (Hayes et al., 2018).

The effect of the boundary conditions is particularly noticeable in the in-plane directions. The expansion of the CASR specimen in the X-direction is notably lower after one year of accelerated testing when compared to the expansion of the UASR specimen in the same direction. The additional restraint of the boundary condition (steel confinement frame) accounts for a 50% reduction in X-direction expansion (Hayes et al., 2018). The boundary condition produces a similar effect on the Y-direction expansion; however, the additional reduction of expansion due to the confinement is less than that of the X-direction reduction due to the longer span of the steel confinement frame resisting Y-direction expansion.

This anisotropy in the macroscopic expansion is likely to be related to a preferred orientation of the ASR-induced cracks under local stress. Due to the specific geometry of the reinforcements, the stress distribution is non-uniform across each specimen, making it difficult to analyze the cracking distribution and therefore the anisotropy in macroscopic strain without relying on nonlinear numerical analysis. This experimental campaign represents a good opportunity to test and validate structural models for ASR, notably to check whether such a model can capture the anisotropy of the macroscopic strain.

8.1.4 Effect of Confinement on Material Properties

Figure 47 and *Figure 48* show the respective evolution of the relative modulus of elasticity, and compressive strength (normalized by the values of these properties at 28 days after casting) with the averaged expansion measured on the corresponding large specimens. It must be noted that the expansion of the large specimens is not necessarily representative of the expansion of cylinders. However, the measured expansion on the large specimens is used as a reference to compare the behavior of the CASR and UASR cylinders.

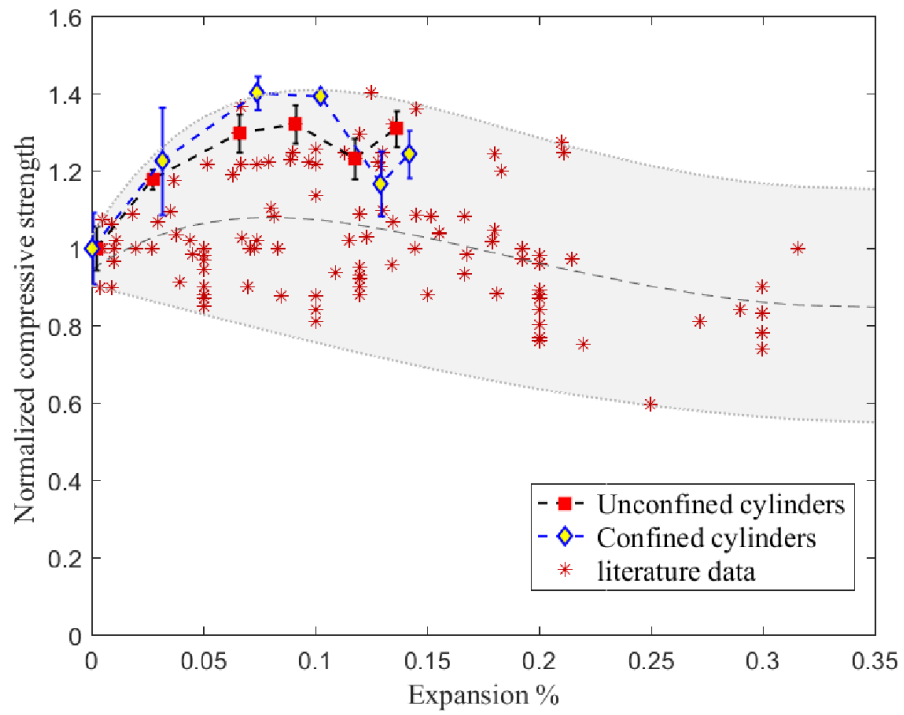


Figure 47: Change in relative compressive strength with ASR expansion (Hayes et al., 2018)

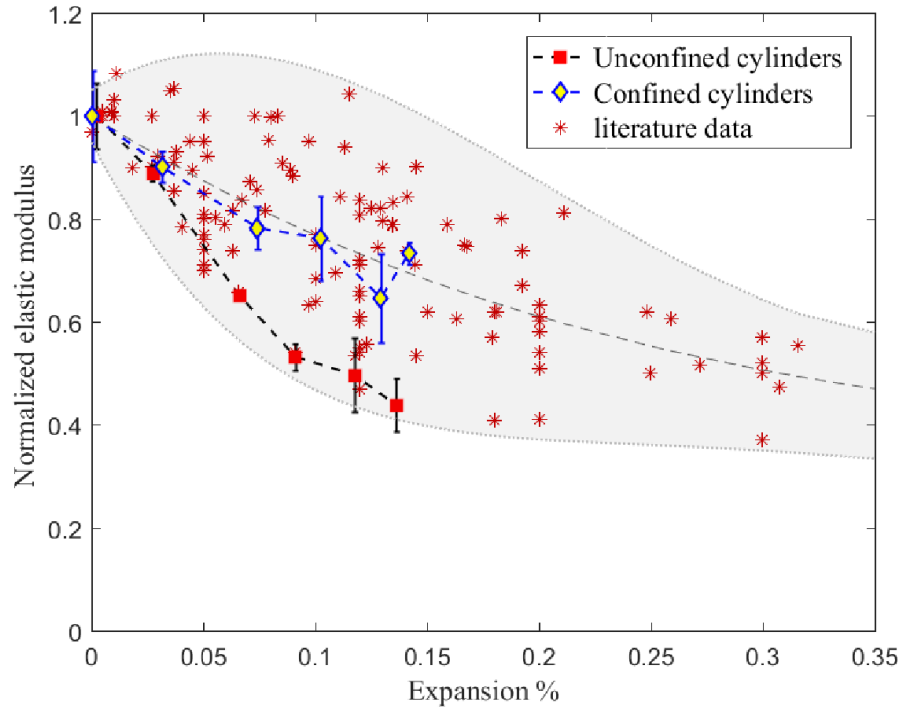


Figure 48: Change in relative elastic modulus with ASR expansion (Hayes et al., 2018)

Figure 48 compares the evolution of elastic modulus in the confined and unconfined cylinders. It can be seen that the stiffness degradation in the UASR cylinders was significantly higher than that in the CASR cylinders. While the relative modulus of elasticity of the UASR cylinders decreased to 43% at a linear expansion of 0.12%, the CASR relative modulus decreased to 63% of the relative modulus of elasticity at an estimated linear expansion of 0.13% and slight recovery was noticed afterward (Hayes et al., 2018). This behavior may be attributed to the contribution of the lateral confinement stress in reducing the loss of the elastic modulus (Gautam et al., 2017).

As shown in **Figure 47**, both the UASR and CASR cylinders showed a remarkable gain in compressive strength until an estimated expansion of about 0.10% and followed by noticeable reduction at an expansion of $\approx 0.12\%$ before a partial gain was observed. As two competing mechanisms, the ongoing hydration of cement and ASR damage, were progressing during early stage of expansion, the increase in compressive strength due to cement hydration seemed to overcome the loss of strength due to ASR (S Multon, Seignol, & Toutlemonde, 2005; Na, Xi, Ou, & Saouma, 2016). At later stage (i.e., for expansion $> 0.1\%$), the ASR damage effects seemed to be dominant. It must also be noted that the compressive strength was affected by the direction of ASR-induced damage, the CASR cylinders (where cracking is primarily oriented parallel to the loading direction) showed higher strength values than that of the UASR, except for the last measurement.

The slight recovery of the mechanical properties at a late stage of ASR expansion was reported in the literature (Ahmed et al., 2003; Gautam, 2016; R. N. Swamy & Al-Asali, 1988). This recovery can be attributed to the continuation of cement hydration process (R. N. Swamy & Al-Asali, 1988), or to the transformation of ASR gel in cracks into a more calcium-rich gel (eventually resembling C-S-H gel) which can contribute to the concrete regaining strength and stiffness (Gautam, 2016).

8.2 Discussion of Acoustic Emission NDE

8.2.1 Advantages and Limitations

Data collected in this research has shown that acoustic emission can be used as a nondestructive evaluation technique to qualitatively monitor the progression of ASR in nuclear thick reinforced concrete. This method was able to monitoring the full thickness of the specimens (1 meter). The AE NDE parameter, cumulative signal strength, can serve as a qualitative measurement that could be used as an indicator for the level of expansion. The intensity analysis of the AE data provides a level of severity accompanied by historic index that could possibly be used to qualitatively assess the presence of ASR in a concrete structure. While this application has not yet been tested on this research data, with sufficient instrumentation, acoustic emission could also be used to locate event sources (energy associated with the opening of cracks) which could possibly be used to provide insight on the location of internal damage.

While acoustic emission could possibly provide benefits as a nondestructive monitoring technique of reinforced concrete affected by ASR, the technique does have some limitations or specific requirements that may be demanding for use by the nuclear power plant industry. First, the method requires continuous passive monitoring which means that several sensors and a monitoring system must be maintained for the duration of the evaluation. The AE monitoring equipment are relatively expensive when compared to conventional strain or deformation monitoring. Second, the method is susceptible to ambient noise. While the ambient noise can be somewhat negated by use of a “dummy” specimen (a nearby smaller specimen known to be made of sound concrete used to capture ambient “noise” of the environment), the presence of outside events other than crack formation requires that the data be filtered to remove events which are not relevant to the monitoring. Third, because of the required data filtering and complexity of the collected data, an experienced operator or software is required to analyze the data.

8.2.2 Comparison with Permanent Strain Monitoring Data

Based on the results obtained for the large-scale specimens, acoustic emission is capable of obtaining a cumulative signal strength parameter that can qualitatively estimate the progression of crack formations

and is similar to the progression of volumetric expansion as shown in Figure 4.3.3. While the cumulative signal strength is more of a qualitative measurement, it could possibly serve as an indicator for the presence and progression of ASR. The intensity analysis also showed differences in the reactive specimens and control specimen. These two results from this study show that AE can be used to qualitatively detect the presence and progression of damage due to ASR in nuclear thick reinforced concrete.

8.3 Discussion of Digital Image Correlation NDE

8.3.1 Advantages and Limitations

Digital image correlation was used to collect strain data on the surface of the UASR specimen. DIC is a non-contact full field method without any preinstalled sensors or wiring. This method, however, is only able to evaluate the strain on the surface. The pattern application can be simple and relatively inexpensive. The DIC provided a strain history of the monitoring area with a complete strain field. This strain field could possibly be used to detect location of cracks as they are forming. With the strain images, any expansion could be detected over time possibly identifying the need to investigate for the presence of ASR.

While the pattern application can be inexpensive, the camera equipment and software can be expensive requiring an up-front investment. Additionally, the procedure for capturing images and analyzing the strain images could require a trained individual. Some independent companies do provide DIC as a service. Monitoring of an in-field nuclear structure with DIC would require periodic images to be taken to detect any expansion. Additionally, over long periods of time, the pattern is susceptible to degradation. Once the pattern is lost, reapplication of the pattern may become necessary which would essentially “re-zero” data collection for any measurements in the future. The images taken of the degraded pattern could not be used to determine the cumulative strain after a new pattern was applied.

8.3.2 Comparison with Permanent Strain Monitoring Data

The DIC calculated strains on the concrete surface are somewhat comparable to embedded strain measurements nearer to the surface (about 25 cm deep into the concrete); however, DIC calculated strain on the surface tend to be larger (by about 50%) than embedded strain measurements at the plateau of measured expansion.

8.4 Discussion of Nonlinear Ultrasonic (NLU) Rayleigh Surface Waves

8.4.1 Advantages and Limitations

The NLU Rayleigh surface waves method was performed within 3 days each at three different testing periods approximately one month apart from each other. This NDE technique does not require any permanent monitoring equipment attached to the concrete. The NDE systems are portable and can simply be brought to the monitoring site having measurements completed with a relatively short time. The technique is extremely sensitive to small changes in concrete at the microscale level. As such, it might be suitable for early detection of ASR before any visible signs are apparent.

Because the technique utilizes nonlinear ultrasonic waves, the method is limited to microscale damage. Once damage is easily observable on the surface, the technique will no longer work. This limitation could be overcome by utilizing a method with linear ultrasonic or some sort of nonlinear/linear ultrasonic wave combination. The investigation depth of this method is limited to 52 mm (Kim et al., 2018) which means that likely only the concrete cover can be investigated. Also, ASR-induced cracking

as well as shrinkage cracking leading to microscale damage causes an increase in the NDE parameter which may make it difficult to distinguish between the two phenomena using this technique alone.

8.4.2 Comparison with Permanent Strain Monitoring Data

As shown in *Table 9* through *Table 11s*, the measured nonlinearity parameter increased with increasing measured expansion from permanent monitoring showing good correlation with the NDE parameter and increasing ASR cracking/microscale damage. However, during the last measurement, the expansion was likely high enough that microscale damage had transitioned to the macroscale rendering the technique ineffective at measuring damage.

8.5 Discussion of Diffuse Ultrasonic Waves (DUW)

8.5.1 Advantages and Limitations

This method could successfully investigate the full thickness of the specimens (1 meter). Because the monitoring equipment was installed after the majority of ASR expansion had occurred, the technique was instead used to try and find some relationship for detection of preexisting damage. With some additional research, the effect of preexisting damage on relationship of NDE measured parameters and temperature could possibly be used to assess the presence of preexisting damage even without previous knowledge of a concrete structure. Additional research will be necessary to form this conclusion.

The technique, as used in this research, is a form of permanent NDE monitoring. As a result, permanent equipment must be attached to the concrete for evaluation.

8.6 Applications of NDE Methods for Detecting/Assessing ASR in NPP Concrete Structures

Acoustic Emission (AE): Acoustic emission can be used as a permanent nondestructive evaluation monitoring system that is capable of detecting the progression or presence of cracking/damage typically associated with ASR-induced expansion near the surface or within the bulk of concrete. The monitoring system would require permanent sensors and wiring with a data collection system.

Digital Image Correlation (DIC): Digital image correlation can be used as a partially permanent monitor the surface strain of concrete. DIC would be able to detect the presence of ASR or other degradation mechanism by observing the presence of expansion attributed to it. The monitoring system would be best suited for application in a controlled environment to prevent degradation of the applied paint pattern on the surface of the concrete. The monitoring system would require a permanent paint pattern on the surface of the concrete. The technique would also periodically require sophisticated camera technology and software for image capturing and data analysis.

Nonlinear Ultrasonic Rayleigh Surface Waves (NLURSW): Nonlinear ultrasonic Rayleigh surface waves can be used as a nonpermanent nondestructive evaluation monitoring system to monitor the near surface of concrete for microscale damage. This method would be best suited for monitoring of concrete for ASR before any visible damage is observable. Once damage is visible, this technique is no longer effective.

Diffuse Ultrasonic Waves (DUW): Diffuse ultrasonic waves can be used as a permanent or nonpermanent nondestructive evaluation monitoring system to monitor the bulk of concrete for changes in propagated wave properties. The monitoring system would require either permanent or nonpermanent

sensors and wiring with a data collection system. Pending additional research, there is potential for this method to detect the presence of pre-existing damage in concrete.

9. Conclusions and Prospective Work

Three large-scale specimens, representative of concrete structural member's thickness and reinforcement ratio without transverse reinforcement found in LWRs NPPs, were fabricated, heavily instrumented, and monitored under controlled accelerated ASR conditions at 38°C and 95% RH. Analysis of the monitoring and NDE data leads to the following conclusions and significant observations:

- The different types of deformation instrumentation, i.e. long-gauge fiber optics or embedded transducers have yielded comparable and dependable expansion measurements despite the severity of the operating conditions, i.e. moderate temperature, high humidity, and high alkalinity.
- Visible surface cracking was not evident on the CASR specimen even with Z-direction expansion exceeding 0.3%. Given that acoustic NDE methods are most influenced by the onset of ASR damage, the observations of the CASR specimen, highlight the need to monitor critical NPP structures before visible evidence of damage appears at the surface, and support the concept that online monitoring of these structures using acoustic methods can provide information not available from visual inspection.
- Surface cracking is not indicative of internal ASR-induced damage or expansion for concrete structures where reinforcement layout or confinement drives expansion primarily in an unobservable plane direction. This potentially allows ASR to cause significant distress to the structure without any visible evidence of its presence.
- Several NDE techniques were used to successfully monitor the progression of ASR induced expansion and damage when compared with data obtained from permanent strain and deformation monitoring. The demonstration of these techniques shows that NDE could be used to successfully monitor the progression of ASR-induced damage or potentially evaluate the presence of ASR in a structure. NDE techniques are accompanied with their own strengths, weaknesses, and limitations associated with monitoring of concrete structures for ASR. The most suitable technique must be selected for a particular purpose.
- Both reinforcement layout and boundary conditions cause highly anisotropic expansion pointing to the need for advanced structural models capable of capturing expansion anisotropy for analysis of in-field behavior.
- Destructive testing will be performed to determine the residual shear capacity of the concrete specimens. The testing plan and results will be detailed in a later report.

10. References

- Abdelrahman, M., ElBatanouny, M. K., Ziehl, P., Fasl, J., Larosche, C. J., & Fraczek, J. (2015). Classification of alkali-silica reaction damage using acoustic emission: A proof-of-concept study. *Construction and Building Materials*, 95, 406-413.
- ACI Committee. (2014). 318, Building Code Requirements for Structural Concrete (ACI 318-14) and Commentary (ACI 318R-14). *American Concrete Institute, Farmington Hills, MI*, 519.
- Ahmed, T., Burley, E., Rigden, S., & Abu-Tair, A. I. (2003). The effect of alkali reactivity on the mechanical properties of concrete. *Construction and Building Materials*, 17(2), 123-144.
- Anay, R., Soltangharai, V., Assi, L., DeVol, T., & Ziehl, P. (2018). Identification of damage mechanisms in cement paste based on acoustic emission. *Construction and Building Materials*, 164, 286-296.
- ASTM, E. (2006). Standard terminology for nondestructive examinations.
- ASTM, I. (2004). ASTM C496/C496M-11 Standard Test Method for Splitting Tensile Strength of Cylindrical Concrete Specimens. West Conshohocken, PA: ASTM International.
- ASTM, I. (2014). ASTM C469/C469M-14 Standard Test Method for Static Modulus of Elasticity and Poisson's Ratio of Concrete in Compression. West Conshohocken, PA: ASTM International.
- ASTM, I. (2016). ASTM C39/C39M-16b Standard Test Method for Compressive Strength of Cylindrical Concrete Specimens. West Conshohocken, PA: ASTM International.
- Bracci, J. M., Gardoni, P., Eck, M. K., & Trejo, D. (2012). Performance of lap splices in large-scale column specimens affected by ASR and/or DEF. *Rep. 0-5722, 1*.
- ElBatanouny, M. K., Ziehl, P. H., Larosche, A., Mangual, J., Matta, F., & Nanni, A. (2014). Acoustic emission monitoring for assessment of prestressed concrete beams. *Construction and Building Materials*, 58, 46-53.
- Farnam, Y., Geiker, M. R., Bentz, D., & Weiss, J. (2015). Acoustic emission waveform characterization of crack origin and mode in fractured and ASR damaged concrete. *Cement and Concrete Composites*, 60, 135-145.
- Gautam, B. P. (2016). *Multiaxially loaded concrete undergoing alkali-silica reaction (ASR)*. University of Toronto (Canada).
- Gautam, B. P., Panesar, D. K., Sheikh, S. A., & Vecchio, F. J. (2017). Effect of Multiaxial Stresses on Alkali-Silica Reaction Damage of Concrete. *ACI Materials Journal*, 114(4), 595.
- Ge, M. (2003). Analysis of source location algorithms: Part II. Iterative methods. *Journal of Acoustic Emission*, 21(1), 29-51.
- Giaccio, G., Zerbino, R., Ponce, J., & Batic, O. R. (2008). Mechanical behavior of concretes damaged by alkali-silica reaction. *Cement and Concrete Research*, 38(7), 993-1004.

- Glisic, B., Hubbell, D. L., Sigurdardottir, D. H., & Yao, Y. (2013). Damage detection and characterization using long-gauge and distributed fiber optic sensors. *Optical Engineering*, 52(8), 087101.
- Grosse, C. U., & Ohtsu, M. (2008). *Acoustic emission testing*: Springer Science & Business Media.
- Hayes, N. W., Gui, Q., Abd-Elssamd, A., Le Pape, Y., Giorla, A. B., Le Pape, S., Ma, Z. J. (2018). Monitoring Alkali-Silica Reaction Significance in Nuclear Concrete Structural Members. *Journal of Advanced Concrete Technology*, 16(4), 179-190.
- Herrmann, N., Niklasch, C., Kiefer, D., Gerlach, L., Le Pape, Y., & Fortier, S. p. (2008). *PACE 1450: An Experimental Test Setup for the Investigation of the Crack Behaviour of Prestressed Concrete Containment Walls*. Paper presented at the 16th International Conference on Nuclear Engineering.
- Hsu, N. (1981). Characterization and calibration of acoustic emission sensors. *Mater. Eval.*, 39, 60-68.
- Inaudi, D. (1997). *Fiber optic sensor network for the monitoring of civil engineering structures*. Verlag nicht ermittelbar.
- Kim, G., Park, S., Kim, J.-Y., Kurtis, K. E., Hayes, N. W., & Jacobs, L. J. (2018). Nonlinear Rayleigh surface waves to characterize microscale damage due to alkali-silica reaction (ASR) in full-scale, nuclear concrete specimens. *Construction and Building Materials*, 186, 1114-1118.
- Kobayashi, Y., & Shiotani, T. (2016). Computerized AE Tomography *Innovative AE and NDT Techniques for On-Site Measurement of Concrete and Masonry Structures* (pp. 47-68): Springer.
- Larive, C., Laplaud, A., & Joly, M. (1996). *Behavior of AAR-affected concrete, experimental data*. Paper presented at the Proc. 10th ICAAR, Melbourne Australia.
- Lokajiček, T., Přikryl, R., Šachlová, Š., & Kuchařová, A. (2017). Acoustic emission monitoring of crack formation during alkali silica reactivity accelerated mortar bar test. *Engineering Geology*, 220, 175-182.
- Maochen, G. (2003). Analysis of source location algorithms Part I: Overview and non~ iterative methods, *J. Acoustic Emission*, 21, 14-24.
- Marzouk, H., & Langdon, S. (2003). The effect of alkali-aggregate reactivity on the mechanical properties of high and normal strength concrete. *Cement and Concrete Composites*, 25(4), 549-556.
- Millard, M. J. (2006). *Effects of Lithium Nitrate Admixture on Early Age Concrete Behavior*. Georgia Institute of Technology.
- Multon, S., Seignol, J.-F., & Toutlemonde, F. (2005). Structural behavior of concrete beams affected by alkali-silica reaction. *ACI Materials Journal*, 102(2), 67.
- Multon, S., & Toutlemonde, F. (2006). Effect of applied stresses on alkali-silica reaction-induced expansions. *Cement and Concrete Research*, 36(5), 912-920.

- Na, O., Xi, Y., Ou, E., & Saouma, V. E. (2016). The effects of alkali-silica reaction on the mechanical properties of concretes with three different types of reactive aggregate. *Structural Concrete*, 17(1), 74-83.
- Rao, M., & Lakshmi, K. P. (2005). Analysis of b-value and improved b-value of acoustic emissions accompanying rock fracture. *Current Science*, 1577-1582.
- Saouma, V. E., Hariri-Ardebili, M. A., Le Pape, Y., & Balaji, R. (2016). Effect of alkali-silica reaction on the shear strength of reinforced concrete structural members. A numerical and statistical study. *Nuclear Engineering and Design*, 310, 295-310.
- Seabrook Station Response to NRC letter to NextEra Energy Seabrook CAL No. 1-2012-002*. (2013). Retrieved from
- Smaoui, N., Bérubé, M.-A., Fournier, B., & Bissonnette, B. (2004). Influence of specimen geometry, orientation of casting plane, and mode of concrete consolidation on expansion due to ASR. *Cement, concrete and aggregates*, 26(2), 1-13.
- Smaoui, N., Bérubé, M., Fournier, B., Bissonnette, B., & Durand, B. (2005). Effects of alkali addition on the mechanical properties and durability of concrete. *Cement and Concrete Research*, 35(2), 203-212.
- Swamy, R. (1994). Alkali-Aggregate Reaction--The Bogeyman of Concrete. *Special Publication*, 144, 105-140.
- Swamy, R. N., & Al-Asali, M. (1988). Expansion of concrete due to alkali-silica reaction. *Materials Journal*, 85(1), 33-40.
- Weise, F. (2012). Innovative measurement techniques for characterising internal damage processes in concrete due to ASR.